JGR Earth Surface

RESEARCH ARTICLE
10.1029/2021JF006467

The Contribution of Sand Ripple and Slope Driven Sediment Flux to Morphologic Change of an Idealized Mound Under Waves

Seok-Bong Lee[1], Meagan E. Wengrove[1], Matthieu A. de Schipper[2], Julia Hopkins[3], Maarten G. Kleinhans[4], and Gerben Ruessink[4]

[1]School of Civil and Construction Engineering, Oregon State University, Corvallis, OR, USA, [2]Faculty of Civil Engineering and Geosciences, Department of Hydraulic Engineering, Delft University of Technology, Delft, The Netherlands, [3]Department of Civil and Environmental Engineering, Northeastern University, Boston, MA, USA, [4]Department of Physical Geography, Faculty of Geosciences, Utrecht University, Utrecht, The Netherlands

Key Points:

- The diffusion of a steep submerged sand mound under unidirectional waves is driven by ripple migration and slope effects
- Mound geometry-driven wave nonlinearities cause a down-slope current that invokes along-ripple sediment avalanching and ripple splitting
- Downslope ripple progression dominates the initial mound diffusion and transitions to lateral ripple migration as the mound slope decreases

Supporting Information:

Supporting Information may be found in the online version of this article.

Correspondence to:

S.-B. Lee,
leeseokb@oregonstate.edu

Citation:

Lee, S.-B., Wengrove, M. E., de Schipper, M. A., Hopkins, J., Kleinhans, M. G., & Ruessink, G. (2023). The contribution of sand ripple and slope driven sediment flux to morphologic change of an idealized mound under waves. *Journal of Geophysical Research: Earth Surface*, *128*, e2021JF006467. https://doi.org/10.1029/2021JF006467

Received 6 OCT 2021
Accepted 23 DEC 2022

Abstract We investigate pathways of sediment diffusion for a Gaussian-shaped sand mound subjected to monochromatic waves. Our unique results nearly close the sediment budget by quantifying each of the sediment transport processes responsible for mound diffusion associated with sediment flux due to slope driven transport and ripple migration. Downslope ripple progression was observed as ripples formed at the mound top advanced down the side slopes in a direction perpendicular to wave propagation. Once ripples formed on the sides of the mounds the ripples became pathways for sediment flux from the top to the bottom of the mound, persisting even after ripples reached the base of the mound as sediment avalanching due to gravity and mound slope. Lateral ripple migration caused ripples to migrate along the sides of the sand mound in a direction parallel to wave propagation. Once ripples reached the base of the mound, lateral migration of ripples caused spreading of sand around the sides of the mound. Lateral ripple migration was largely driven by ripple splitting caused by a large downslope sediment flux from the center of the mound that generated ripples with longer wavelengths than wave orbital hydrodynamics could support. To restore equilibrium between sediment and flow conditions, ripples with longer wavelengths continuously split and migrated laterally around the mound. Our results reflect the importance of slope driven transport, bed fluidization, and ripple dynamics on the larger scale diffusivity and suggest that slope driven and ripple driven sediment fluxes should be more explicitly included in sediment transport formulations.

Plain Language Summary To maintain the shape of our coastlines we nourish our beaches by placing large volumes of sand on the beach itself or slightly seaward of the shoreline. Natural waves and currents then distribute the placed sand. For the purposes of coastal planning, we need to know: How long will the nourishment last? and Where will the sand go? In order to predict the time scale and direction of sand dispersal, we depend on sediment transport parameterizations within coastal change models. However, many sediment transport parameterizations were designed for flat surfaces, while they need to be applied to the slopes of the nourishment mound, which is further covered in ripples. As such, we are likely missing important physical processes associated with the sediment transport of nourishment diffusion. Here we present a laboratory scale experiment with an idealized Gaussian sand mound and observe the mechanisms of sediment transport associated with the re-distribution of the mound sediments on a three-dimensional bathymetry. The measurements show how slope driven sediment transport and sand ripple migration dynamics modify the sediment flux processes important for mound diffusion. The insights are useful for improvement of sediment transport formulations that are used to predict coastal change.

1. Introduction

The shape of our coastline is dynamic. Sediment mounds form in locations of sediment flux convergence and diffuse in locations of sediment flux divergence. Presumably, both convergent and divergent processes occur when the flow field conditions are not in equilibrium with the morphology (Ribas et al., 2015). In the case of modeling morphologic evolution, models often parameterize morphologic change of the bathymetry using coefficients of diffusion (de Vriend, 1987b; Lesser et al., 2004; Moulton et al., 2014). The efficacy of these models and their parameterizations are tested with idealized cases of morphological evolution, such as spreading

of a Gaussian shaped mound under currents and waves (de Vriend, 1987b; Lesser et al., 2004) or infilling of a hole in the surfzone (Moulton et al., 2014). However, many morphologic change models still have error in their prediction (Bosboom et al., 2014; Hewageegana & Canestrelli, 2021; Sherwood et al., 2022) and potentially not coincidentally, morphologic change models do not necessarily consider each sediment transport mechanism that is important for mound spreading. Herein, we build upon past idealized sediment mound diffusion experiments with full characterization of each sediment transport mechanism that contributes to idealized 3D mound diffusion under waves alone. With our observations we were able to fully close the sediment budget of the three dimensional mound spreading via observations of ripple and slope driven transports. Results are important because there are few, if any, studies that are able to fully close the sediment budget in a three dimensional case. The three dimensional nature of the experiments highlight that depending on position around the 3D mound, the key transport processes are variable, which could be important for morphological evolution models and future improvements to diffusion coefficients to accurately predict the change in morphologic shape. Finally, recent field experiments suggest that small scale morphological evolution contributes substantially to larger scale morphologic change (Jones & Traykovski, 2019; Wengrove et al., 2022), this study confirms those findings by fully closing the sediment budget of mound spreading. We quantify the contribution of individual transport mechanics of associated with small scale ripples and variability in mound slope to account for larger scale morphologic change of the three dimensional mound.

Here we use "diffusion" to mean attenuation of relief of sediment forced by local hydrodynamics (i.e., waves). Several studies adopted similar usage of the term diffusion to describe spreading of morphologic features, such as a nourished sand profile (Dean & Dalrymple, 2004; de Schipper et al., 2016), Gaussian-shape dredged hole (Moulton et al., 2014), or shoreline sand waves (Van den Berg et al., 2012). Morphologic diffusion has been studied through numerical modeling and experiments such as investigations of mound diffusion under steady and unidirectional flow to diffusion experiments in more complex flow conditions. The seminal numerical experiments of de Vriend (1987b) used mathematical models to investigate the morphological evolution of a sinusoidal hump under a steady 0.5 m/s current. He argued that even though sediment transport is governed by 2D flow or a quasi-2D flow after depth-averaging (2DH), morphological evolution should be considered three-dimensional because three-dimensional sediment structures propagate in all directions even under the 2D or quasi-2D assumption. An early flume experiment that implemented a sinusoidal-shape sand hump by Hauguel (1979) and mathematical analysis of the hump diffusion by de Vriend (1987b) suggest that quasi-2D depth-averaged models are not valid for sand hump diffusion because key bed properties (e.g., bed slope, bottom roughness) are not considered in the model. For the hump-shaped mound, the bed slope was found to be the most crucial factor for predicting morphological diffusivity. As such, new morphological diffusivity flume experiments and field experiments were carried out to investigate three-dimensional morphological change. Stansby et al. (2009) investigated diffusion of a Gaussian circular mound under long period sinusoidal oscillatory flow conditions and found that ripple formation on the mound top agitates sediment particles within the wake region, which causes greater volume loss than depth-averaged bathymetric models predict, indicating that ripple formation may be significant to mound diffusion. Smith et al. (2017) also carried out laboratory experiments focusing on morphological diffusivity of a submerged sand mound under oblique random waves. They observed mound diffused with an offshore downdrift in the direction of undertow and observed diffusion rates to depend on bed slope (Aagaard et al., 2002; Longuet-Higgins, 1983; Longuet-Higgins & Stewart, 1964); observations indicate that beach slope is important to diffusion. During the same experiments with Stansby et al. (2009), García-Hermosa (2008) investigated mound diffusion under 0.5 m/s steady currents, and observed significant ripple-dominant sediment flux during the most significant periods of mound shape modification. Collectively, the previous mound diffusion experiments (de Vriend, 1987a, 1987b; García-Hermosa, 2008; Hauguel, 1979; Smith et al., 2017; Stansby et al., 2009) suggest (a) that mound diffusion is a 3D process given that the 2DH models poorly represent experimental data for both wave driven and current driven diffusion, and (b) that bottom irregularities, such as ripples, can dominate morphodynamics during three-dimensional mound diffusion.

Here we report on the MOrphological Diffusivity EXperiment (MODEX) that examined mechanisms of three-dimensional sediment diffusion of a Gaussian shaped sand mound subject to waves. As stated, our aim is to quantify the sediment transport mechanisms leading to morphological diffusivity of the three-dimensional mound. We hypothesize that mound diffusion is primarily driven by ripple generation and migration and slope effects under wave-driven flow in the energy regime where bedload transport is of leading order. We look in detail at individual sediment transport mechanisms in order to ultimately suggest how formulations used in large-scale

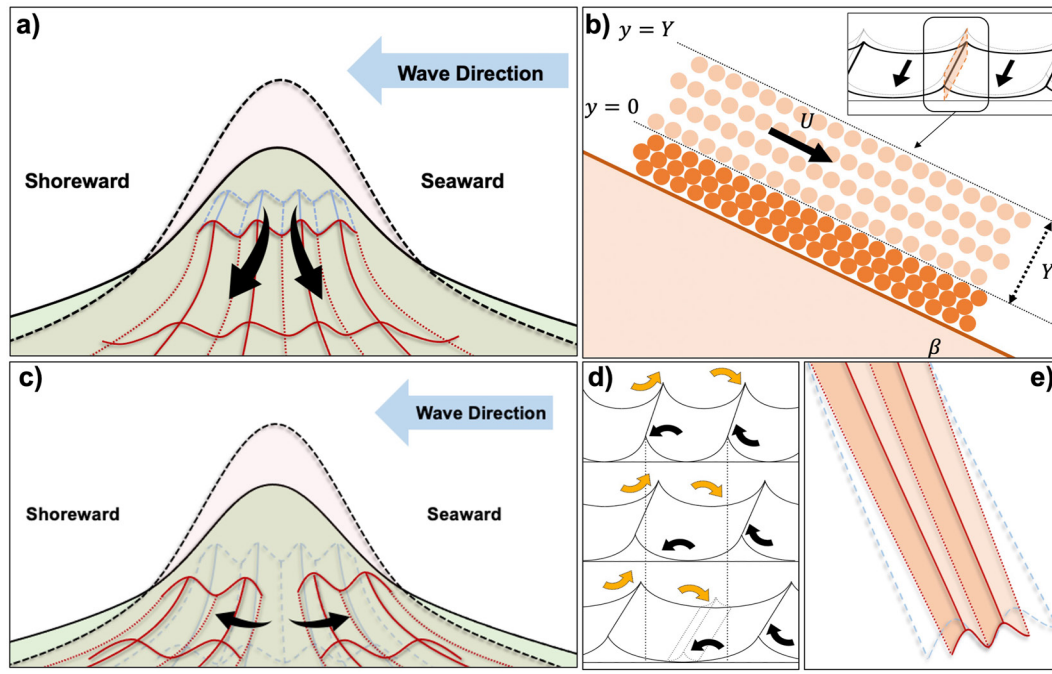

Figure 1. Schematics describing sediment flux mechanisms important for mound diffusion. (a) Downslope ripple progression (form of avalanching), (b) mobile ripple layer avalanching due to gravity, (c) lateral ripple migration, (d) ripple splitting, and (e) ripple shrinking during migration. In panel (b) U indicates mean avalanche velocity, Y is mobile layer thickness, and β is the slope. In panel (d) arrows with a concave-down shape and arrows with a concave-up shape illustrate sediment pick-up and deposition during one wave cycle.

morphologic change models may be improved. Although it is likely that individual mechanisms cannot all be included due to numerical constraints, it may be that each could be better represented to more accurately capture the diffusion process. In the following, the specific transport mechanisms relevant to the study are defined to aid in structuring of the results. To conclude, we outline potential pathways to more holistically represent the contribution of ripple migration and slope driven sediment flux contributions to morphodynamic change in existing models and address the potential influence of scale effects on the study results and conclusions.

1.1. Ripple Mechanics

During bedload transport dominated conditions, sediment flux driven by bedform translation and deformation can contribute to the depositional and erosion patterns in the nearshore (Aagaard et al., 2001; Coco & Murray, 2007; Hay & Mudge, 2005; Saulter et al., 2003; van Rijn, 2007; van Scheltinga et al., 2020; Wengrove et al., 2018). The sediment flux mechanisms important for the diffusion of a three-dimensional sediment mound include ripple migration and propagation (Figures 1a and 1c), ripple growth and decay (Figure 1e), ripple splitting leading to higher rates of lateral migration (Figure 1d), and gravitational influence leading to sediment flux driven by mobile ripple layer avalanching (Figure 1b) (Aagaard et al., 2004; Allen & Collinson, 1974; Dalrymple & Rhodes, 1995; Dietrich & Smith, 1984; Lefebvre et al., 2013; Passchier & Kleinhans, 2005; Ruggiero et al., 2016; van Scheltinga et al., 2020; Winter et al., 2008). Each ripple dynamic described herein and observed through the MODEX experiment has already been observed by previous field and flume experiments (Doucette & O'Donoghue, 2006; García-Hermosa, 2008; Stansby et al., 2009; van Scheltinga et al., 2020). However, unlike previous observations, the MODEX data set quantifies the sediment flux contribution associated with each ripple driven and gravity driven transport mechanism and quantifies the contribution of each sediment flux mechanism to larger scale mound diffusion. Following, we define each sediment flux mechanism in the context of Figure 1.

Ripple migration occurs when the ripple sediment flux is in phase with the ripple shape (Nielsen, 1992); sediment is transported from one side of the ripple and deposited on the other side (Figures 1a and 1c). As such, in subcritical current-driven flows, ripples travel in the flow direction. Under waves, mechanics of ripple migration are understood to be driven by wave-driven currents and wave streaming (Kranenburg et al., 2012), sloping bed

(Wang & Yuan, 2018) or by the orbital motion under asymmetrical and/or skewed waves (Crawford & Hay, 2001; van der Werf et al., 2007). Ultimately, ripple migration is important because it has been observed to drive sediment transport (Masselink et al., 2007; Miles & Thorpe, 2015; Petrotta et al., 2018; Traykovski et al., 1999; Wengrove et al., 2018, 2019, 2022). The use of the general term "ripple migration" in literature often refers to what we refer to herein as "lateral ripple migration." We consider lateral ripple migration to be the process where ripples begin to migrate in the direction perpendicular to their orientation on the mound in the direction parallel to the wave propagation in both the shoreward and the wave maker directions (Figure 1c). Downslope ripple progression is introduced as the process where ripples are initially formed due to agitation of sediments at the top of the mound and then their terminus (or tips) propagate in the direction parallel to the ripple orientation down the side slopes of the mound partially due to gravity and partially due to continued agitation of the bed (Figure 1a).

When ripples form and remain dynamic, there is a portion of the ripple near the crest that remains mobilized by oscillatory motion and released vortices from the ripple crest (Ruggeri et al., 2020). Known as the fluidal zone, this part of the ripple can be inferred to be the mobile layer (Flores & Sleath, 1998; Sleath, 1999; van der Werf et al., 2007). With guidance from literature an assumption can be made that the mobile layer adds to the sediment flux during downslope ripple progression due to slope effects, which is a form of mobile layer avalanching. The slope of the mound can alter sediment diffusion, ripple migration, and ripple formation (Baar et al., 2018). For a sloping bed, the gravitational force parallel to the bed slope will affect bedload sediment transport through the mobile layer. Downslope ripple progression can also occur, and is a form of mobile layer avalanching as the ripple migrates parallel to the crest line down the sides of the mound due to both agitation of the bed and the mound slope. Both downslope progression and mobile layer avalanching contribute to mound diffusion and their flux magnitudes are a function of mound slope. As such, the bed slope must be considered when quantifying morphological diffusivity (Damgaard et al., 1997; Engelund, 1981; Luque & van Beek, 1976). The effect of slope on mound diffusion through the fluidized ripple layer is not well investigated. In the experiments reported here, the feedback between changing mound slope and ripple dynamics are considered in detail.

Ripple splitting is a mechanism where a new ripple is generated between two existing ripples to maintain equilibrium with the flow field (Doucette & O'Donoghue, 2006). As the ripple splits and a new ripple is formed, the split ripple drives migration laterally of all ripples fore and aft of its location, thereby driving sediment flux in both the shoreward and wave maker directions (Allen, 1973, 1976; Baas, 1994; Jerolmack & Mohrig, 2005; Miles & Thorpe, 2015). During ripple splitting under waves, when the spacing between the two ripples is much larger than the water particle orbital diameter d_0, sediment is deposited continuously between the ripples, forming a third smaller ripple and the ripples deform in order to move toward equilibrium with the flow (Figure 1d). The oscillatory flow tunnel experiments of Doucette and O'Donoghue (2006), which tested varying flow periods, flow orbital diameters, and mobility numbers, suggest that equilibrium ripple geometry is a function of flow condition. In oscillatory flow, ripples are said to be orbital when they are in hydrodynamic equilibrium with the ambient waves. Generally, the orbital ripple wavelength, λ, scales linearly with the water particle orbital diameter, d_0, at a ratio of $\lambda/d_0 = 0.65$ for fine sand (Clifton & Dingler, 1984), and decreases to about $\lambda/d_0 = 0.55$ for coarse sand (Ruessink et al., 2015). Ripple splitting changes the ripple geometry of adjacent ripples. To accommodate the emergence of excess sand flowing down the sides of the mound, adjacent ripples in the center of the mound extend in spacing, increase in volume, and decrease in slope. The extended spacing between ripples force the ripples out of equilibrium with the flow field (moving from orbital to suborbital ripples). The sediment transported over the crest of the adjacent ripples can only reach to the center of the trough between the two adjacent ripples, thereby re-instating equilibrium with the generation of a new ripple formed via ripple splitting, and the adjacent bedform scale decreases once again to scale with the flow conditions (Kocurek et al., 2010).

Ripples can also change geometry by growing and/or decaying (Figure 1e) when the ripple sediment flux is out of phase with the ripple shape (Nielsen, 1992; Wengrove, 2018). Ripple growth and decay can occur in wave dominant, current dominant, and combined flow conditions (Doucette & O'Donoghue, 2006; Nienhuis et al., 2014; van Scheltinga et al., 2020; Wengrove et al., 2018). Both laboratory and field studies on planar beds have observed that growth or decay occurs when the ripples "pick up" or "leave behind" sediment, respectively. In the case of a planar bed with low-mobility condition, ripples are considered to be two-dimensional (O'Donoghue et al., 2006), meaning that all ripples will respond equally to a change in the flow conditions. However, the diffusion process is three-dimensional in the case of a sediment mound. For three-dimensional sediment diffusion, ripple geometry is dependent on the mound's surface slope since the flow energy at the bed decreases with depth. As such, ripples at the top of a submerged mound can be larger than those at the bottom. For example, the linear

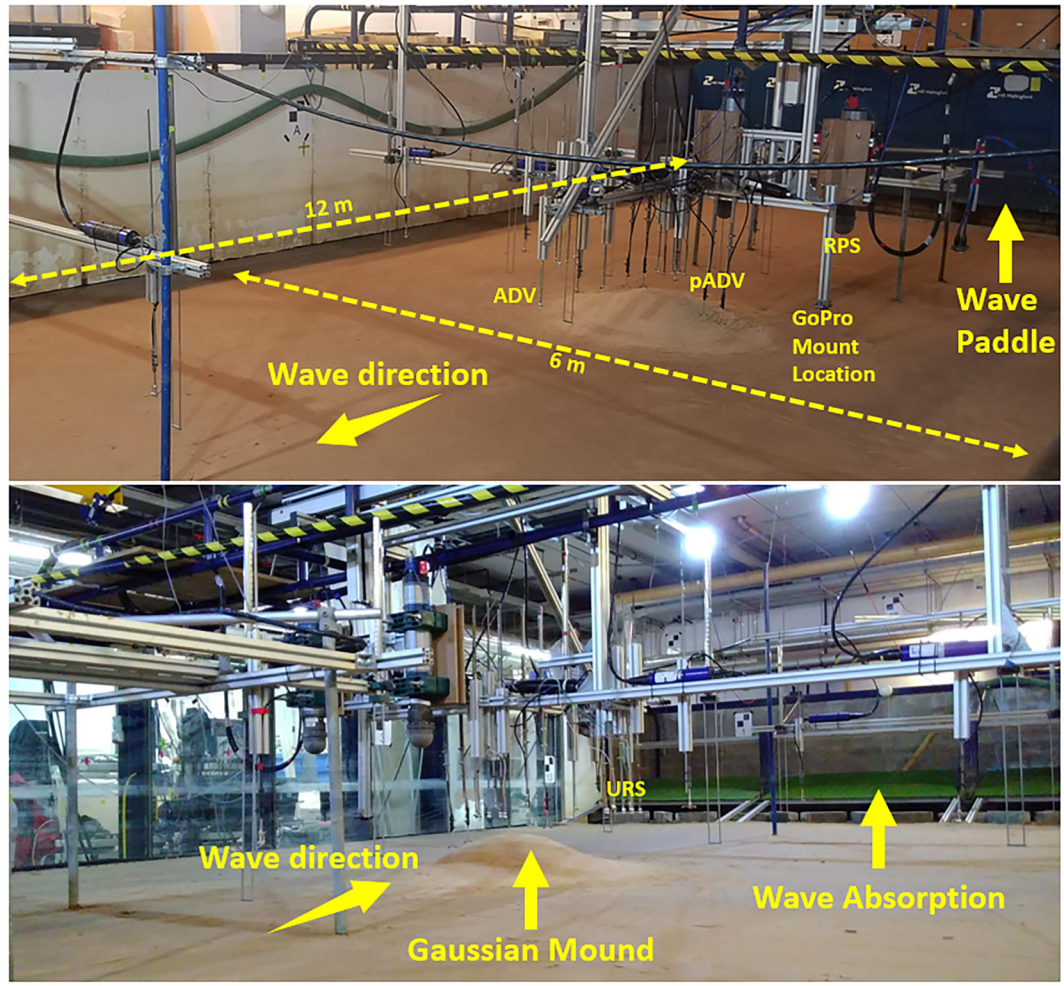

Figure 2. Photos of the Hydralab + Total Environment Simulator flume showing the position of the wave maker and beach, instruments and the Gaussian shape sand mound. Top panel shows wave paddle side (wave maker side) and bottom panel shows beach side (shoreward side).

scaling of orbital ripple wavelength with orbital diameter suggests that ripple wavelength should decrease as a function of mound height due to the decay in orbital diameter as a function of depth.

2. Methods

2.1. Experimental Description

Data were collected during the Hydralab + MODEX laboratory experiment in June of 2018. Experiments were performed in the Total Environment Simulator at the University of Hull (United Kingdom) (see de Schipper et al. (2019) for more detailed experimental setup and test conditions). The flume is 12 m long and 6 m wide and is capable of simulating combined wave-current flows (Figure 2). We created an artificial beach with a rough surface to encourage wave absorption and dissipation and to mitigate wave reflection (Figure 2). During the MODEX experiments a total of nine hydraulic conditions were tested, we focus on two wave conditions to investigate diffusion of a Gaussian shape sand mound for the analysis performed herein (see de Schipper et al. (2019) for more detail on other forcing conditions).

The sand mound was 150 cm diameter and 20 cm high with a 0.215 mm median grain size sand. Herein, we investigate mound diffusion in 40 cm water depth during two monochromatic intermediate depth wave cases (Table 1). Series 1 was composed of 10 sequential runs carried out for a total of 150 min of run time. Series 2

Table 1
Wave and Mobility Conditions, Where $\theta_{2.5} = 0.5 f_{2.5}\rho(A\omega)^2/(\rho(s-1)gd_{50})$, $f_{2.5} = \exp\left[5.213(2.5d_{50}/A)^{0.194} - 5.977\right]$, d_{50} *Is Mean Grain Diameter,* ω *Is Angular Frequency,* ρ *Is Water Density,* s *Is Specific Gravity of Sand (=2.65),* A *Is Semi-Orbital Excursion, and* K_r *Is Wave Reflection Coefficient* (H/H_r) *After Separating Incident and Reflected Waves (Baldock & Simmonds, 1999; Goda, 2010)*

Series number	Number of runs	Length of each run (min)	Wave height (m)	Wave period (s)	$\theta_{2.5}$ at mound bottom	$\theta_{2.5}$ at mound top	kh	K_r
Series 1	10	15	0.11	1.00	0.08	0.13	1.72	0.35
Series 2	9	10	0.14	1.20	0.16	0.22	1.30	0.31

was composed of nine sequential runs carried out for a total of 90 min of run time. Due to time constraints and consistency between series, runs were performed until the mound height decayed to approximately 50% of its original height (de Schipper et al., 2019).

For the purpose of the analysis presented herein, four Nortek Vectrino Profiling ADVs (pADV), two Marine Electronics 3D Ripple Profiling Scanners (RPS), a FARO Focus X330 lidar scanner, 10 Seatek 2 MHz ultrasonic altimeters (ultrasonic range sensor (URS)) and a GoPro camera were used to investigate morphodynamic and hydrodynamic characteristics of sand mound diffusion (Figure 3). The pADVs measured a profile of velocity over 35 mm of vertical range at 1 mm resolution. Two RPS with 0.5 m spacing were used for measuring the subaqueous mound shape between runs; each RPS had a resolution of approximately 1 cm just below the scanner at a range of 0.4 m, and a 1.7 cm resolution at 60° from the center. Sonar scans were repeated to create six overlapping locations to resolve the full sediment mound shape between each run. Lidar scans were collected before the flume was filled with water and after the entire series once the flume was drained slowly so as to not disturb the sediment surface. The lidar has a resolution of 3 mm at 10 m distance (de Schipper et al., 2019). Each URS collects time series of bed elevation change at a frequency of 1 Hz directly below the 1 cm diameter transducer with 1.8° beam width. The URS were grouped in 5 s to track the directionality of the sand ripple migration using cross correlation between the individual URS sensors when the water clarity was poor. Sediment

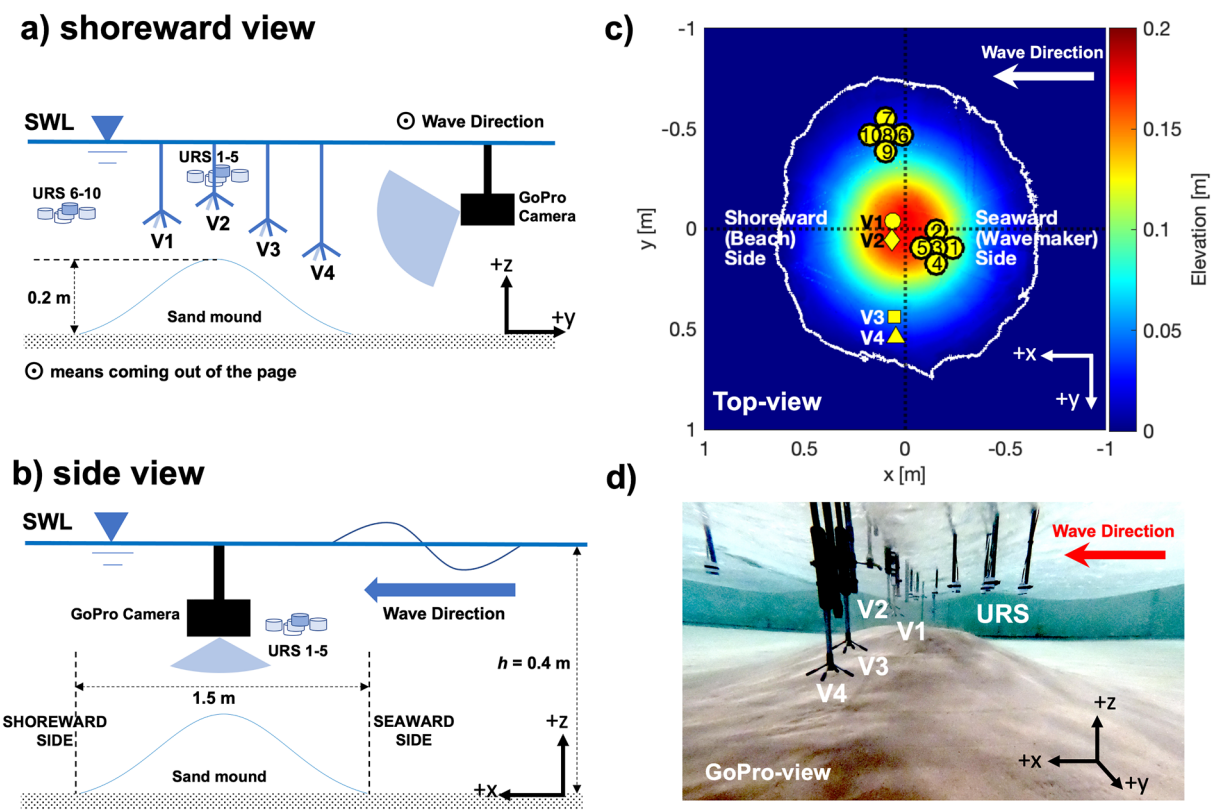

Figure 3. Schematic of the MOrphological Diffusivity EXperiment experimental setup. (a) Shoreward view of sand mound. (b) Side view of sand mound. (c) Top view of sand mound with lidar scan data from pre-series. Colorbar shows initial mound elevation and white solid contour illustrates zero-elevation of the mound. Instruments (4 Profiling ADVs [pADV] and 10 ultrasonic range sensor [URS]) are also shown. (d) GoPro view with pADV (V1–V4) and URS locations.

morphodynamics were documented during each run using a GoPro camera mounted underwater facing the side of the mound. The GoPro camera captured 12 megapixel images with a 30-s sampling interval to monitor ripple dynamics on the sand mound.

2.2. Hydrodynamics

Profiles of wave-driven mean currents and orbital statistics are analyzed using the pADV measurements. All pADV measurements were decomposed into mean ($\bar{u}$) and wave ($\tilde{u}$) components ($u = \tilde{u} + \bar{u}$), and all wave statistics were phase-averaged over 30 s to pair with morphological sampling from GoPro timelapse images. The wave components of velocity were found using a down-crossing method to divide the regular wave signal in the x-direction. Same crossing positions in time were used to divide the y-directed wave velocities. The individual waves were phase averaged to determine $\tilde{u}$ and $\tilde{v}$. All pADV time series used for data analysis were measured at a fixed near-bed vertical location of 4 mm above the bed (i.e., each pADV profile was adjusted to distance from boundary coordinates where the boundary was found using the instrument amplitude return). We adjusted the elevation of each pADV after each run so that the pADV profile was always intersecting with the boundary. The wave component was found using a zero-crossing method. The wave orbital diameter, d_0, is estimated following Maier and Hay (2009),

$$d_0 = \frac{2\tilde{u}_{1/3}}{\omega_p}. \tag{1}$$

where $\tilde{u}_{1/3}$ is the significant wave orbital velocity, which is calculated from the root-mean square of the wave orbital velocity time series ($\tilde{u}_{1/3} = 2\tilde{u}_{rms}$), and ω_p is the angular frequency at the peak of the wave energy spectrum.

2.3. Image Processing

Each image from the GoPro camera contains information about ripple geometry with the exception of ripple height, which cannot be obtained using image rectification. With the 2-D geometry reconstruction of the ripples, ripple wavelength, and morphodynamical features, such as ripple generation and migration, can be estimated from each image. The process of image rectification uses a transformation matrix to convert the two-dimensional coordinates of each oblique image to a real-space coordinate system. The transformation matrix is determined from the known intrinsic parameters of the camera and the real-world coordinates of five ground control points (see Lee et al. (2019)).

The recovered two-dimensional real coordinates of each pixel at the mound elevation under the pADVs were extracted to compare the boundary layer hydrodynamic data to the corresponding morphodynamics. The extracted pixel data, organized as time-stack plots, were used to estimate ripple migration rates. Since z-coordinates cannot be recovered from the GoPro images, images were draped over linearly interpolated elevations from lidar and sonar scan measurements (Figure 4) to roughly recover the vertical coordinates of the mound.

When processing the hydrodynamic measurements, the time series of the first run was decomposed into wave and current components by phase averaging each 90-s time interval, giving a total of 10 phase averaged wave velocity and residual current estimates over the first run. Remaining runs in the series were decomposed and averaged for the full run. The reason for this scheme is because the mound went under dramatic change over the first run. For the current driven component, error was placed on each measurement using a ±standard deviation.

2.4. Wavelet Analysis

To observe ripple formation and migration, Fourier analysis is used to compute the power spectrum as a function of spatial wavenumber (inverse of ripple wavelength). The peak spatial wavenumber with a maximum power spectral density corresponds to the dominant ripple wavelength. Wavelet analysis is used to provide information on both the spatial location and the morphologic scale of the a non-stationary spatial time series (Cataño-Lopera et al., 2009; Gutierrez et al., 2013; Raja et al., 2002). We use the Morlet wavelet form (Farge, 1992) where a complex exponential term is used as a carrier and it is multiplied by a Gaussian window. For the admissible condition, where the function has zero mean and is localized in both the time and frequency domains, the non-dimensional frequency of the Morlet wavelet, $\omega_0 = 6$ was used (Farge, 1992). The Morlet wavelet is given by

$$\psi_0(\eta) = \pi^{-1/4} e^{i\omega_0\eta} e^{-\eta^2/2} \tag{2}$$

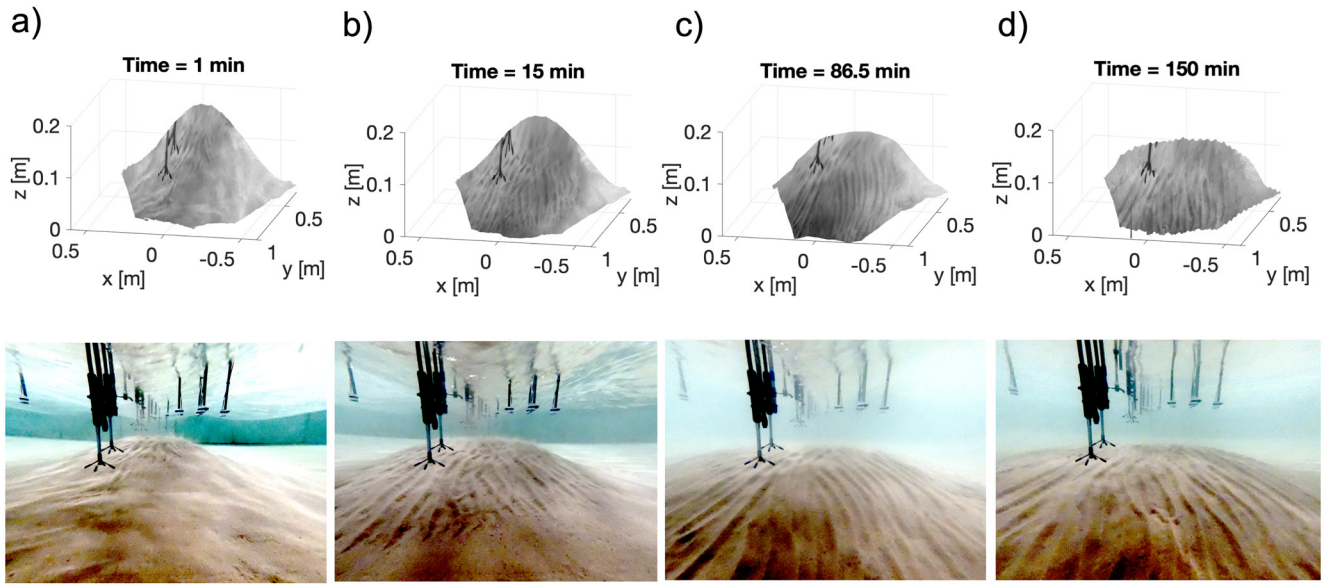

Figure 4. (a–d) Original GoPro images are rectified with Ground Control Points, lidar, and Ripple Profiling Scanners data. Rectified images of sand mound (top) and corresponding raw GoPro image (bottom).

where ω_0 is the non-dimensional frequency and η is the non-dimensional time parameter. The discrete wavelet transform $WT_n(a)$ is estimated by convolution of the inverse Fourier transform of the product,

$$WT_n(a) = \sum_{k=0}^{N-1} \hat{x}_k \hat{\psi}^*(a\omega_k) e^{i\omega_k n\delta x} \tag{3}$$

where n is the space index, a is the wavelet scale, ω_k is the angular frequency, δ_x is the space interval, x_n is the discrete sequence, $\hat{x}_k$ is the amplitude of the Fourier coefficients of the discrete sequence x_n, and ψ^* is a complex conjugate of the carrier wavelet (Cataño-Lopera et al., 2009). By using the wavelet transform, which is composed of real and imaginary parts, the wavelet power spectrum can be estimated by

$$|WT_n(a)|^2 = \sum_{n=0}^{N-1} WT_n^*(a) WT_n(a) \tag{4}$$

where $WT_n^*(a)$ is the conjugate of $WT_n(a)$. The wavelet power spectrum on each ripple wavelength domain can give us the location and amplitude of each power spectrum, which illustrates the dominant wavelength. Detailed methods of the wavelet transform are introduced by Torrence and Compo (1998). Wavelet analysis was applied to each spatial time series of crest position of the ripple. At each spatial location the dominant wavenumber was determined based on the location of the maximum power spectral density and the dominant ripple wavelength was estimated as the inverse of the peak wavenumber.

2.5. Ripple Migration Rate

Lateral ripple migration was measured by tracking the parallel crest lines of the ripples (Figure 1). Lateral migration is influenced by the mound shape evolution (e.g., slope, near-bed hydrodynamics), and so it is not exactly parallel to the propagating oscillatory waves. Three different instruments were used to capture the variability in lateral migration rates around the mound. Using the GoPro images, time-stack plots of cross-sectional pixel intensity at each elevation along the mound (each y-position of Figures 4a–4d; see Figure 9b e.g.,) was used to estimate migration rates. Each crest position could be identified and extracted from the time-stack plots where the slope of the extracted crest lines is the ripple lateral migration rate. Additionally, the bottom tracking data from the URS and pADV were used to estimate lateral migration rates directly under those instruments. Time between the passing of each ripple crest and the corresponding ripple wavelength at that mound elevation determined through the wavelet analysis were used to estimate migration rates. All migration rates are measured values, which are combination of contribution of mound slope and near-bed hydrodynamics.

Downslope ripple progression (downslope movement of the ripple in longitudinal direction) rates were measured by tracking the downslope ripple terminus (tip) location (Figure 1a), as such the distance between the ripple terminus in sequential GoPro images was measured and divided by the time between the images. The coverage area of the GoPro image is not large enough to include the whole mound, thus at some point the termini are outside the GoPro image frame. Therefore, the distance between the final accretion contour and the position of the downslope ripple terminus after the ripple terminus leaves the field of view (run 3 in wave Series 1) is divided by the corresponding time to determine the downslope ripple progression rate after run 3.

2.6. Volumetric Sediment Flux Estimates

2.6.1. Ripple Migration

To quantify the contribution of sediment flux driven by lateral ripple migration to mound diffusion, the following formulas are introduced. We define the time-dependent sediment flux (q_b) due to lateral ripple migration using the one-dimensional sediment continuity equation and assuming a triangular ripple shape as,

$$q_b = -n\frac{\eta}{2}V_{mig} \tag{5}$$

where η is height of the ripple, V_{mig} is the ripple migration rate, and n is the sediment volume fraction (Jones & Traykovski, 2019; Simons et al., 1965). The contribution of ripple migration to volumetric bedload sediment transport is estimated using Equation 5.

The downslope ripple progression was estimated by again assuming a triangular ripple shape and measuring migration rates by tracking the ripple terminus (tip) propagating downslope through a threshold contour defined in Section 2.6.4.

2.6.2. Mobile Layer Avalanching

Using the average ripple geometry along the threshold contour with an estimated downslope-directed sediment transport velocity of the mobile layer, we can estimate the contribution of mobile layer avalanching to mound diffusion. Bagnold (1954) suggests empirical shear stress formulas for mobile layer avalanching that consider both the particle shape and the dominant flow regime. Bagnold (1954) introduced two different regimes for avalanching. One is inertial regime avalanching where the domain of interest is not submerged in water, and the other is the viscous regime avalanching where the domain of interest is submerged into a fluid, such as water. Hence, for our subaqueous sand mound, we used the gravity-driven avalanching formula for the viscous case. For the viscous regime, the shear stress is given by

$$\tau_v = (1 + C_g)\left(1 + \frac{C_g}{2}\right)\mu\left(\frac{dU}{dy}\right) \tag{6}$$

where τ_v is the grain shear stress in the viscous dominant region, μ is the dynamic viscosity of the fluid medium, U is the mean avalanching velocity, and C_g is the linear grain concentration, which is defined as the ratio between the grain diameter (D) and the free distance (b) between each grain particles (D/b). Equation 6 is equated with an expression of shear stress by Sleath (1994) for an inclined slope,

$$\tau = (\rho - \rho_f)g\sin\beta C y \tag{7}$$

where $\tau = \tau_v$, ρ_f is the density of fluid, y is the vertical distance from a fixed bed, β is the slope angle, and C is grain concentration ($= C_0/(1/C_g + 1)^3$ where C_0 is the maximum possible grain packing concentration). With Equations 6 and 7, Allen (1970) introduced an equation for the viscous flow condition of fine sand,

$$U = 0.00063\frac{(\sigma - \rho)g\sin\beta}{\mu}Y^2. \tag{8}$$

where σ is the material density, ρ is the density of water, μ is the dynamic viscosity, β is the bed slope angle, and Y is the mobile bed thickness. The estimated mean avalanching velocity is applied to the mobile layer thickness based on ripple height and is used to estimate the volumetric sediment flux (see Text S1 in Supporting Information S1). Although the mobile layer thickness is generally variable with the flow field, ripple mobile layer thickness has been observed to be approximately half of the ripple height (Wengrove, 2018). In this study, we use half of the ripple height to estimate mobile layer thickness. Hence, we estimate the sediment flux due to the mobile layer avalanching as follows,

$$q_{b,avlch} = \frac{1}{2}\eta U \tag{9}$$

2.6.3. Ripple Shrinking

Assuming that ripple geometry changes linearly, a change in ripple geometry drives a change in ripple volume. As the ripples propagate down the side slopes of the mound they decrease in sediment volume to scale with the local wave hydrodynamics (which are less energetic in the deeper waters), we refer to this process as ripple shrinking. Based on linear wave theory ($d_0 = H/\sinh(kh)$, where d_0 is orbital diameter, H is wave height, k is wavenumber, and h is water depth), as a ripple migrates from the top to the bottom of the mound, the water depth increases 0.15–0.2 m, and as such, the ripple wavelength should decrease approximately 2–3 cm ripple wavelength decrease under the given wave conditions. Ripple shrinking can occur both in the lateral and downslope directions. When ripples migrate laterally ($\pm x$ direction—along tank), a change in ripple volume and its migration rate are given by

$$\frac{d\overline{V}}{dx} = n\frac{dA}{dx}L = n\frac{d\left(\frac{1}{2}\eta\lambda\right)}{dx}L \tag{10}$$

$$\frac{dx}{dt} = V_{mig,la}. \tag{11}$$

where $\overline{V}$ is the ripple sediment volume, A is cross-sectional area of ripple, L is the length of the ripple crest, n is sediment volume fraction, η is ripple height, λ is ripple wavelength, and $V_{\text{mig,la}}$ is lateral ripple migration rate. Combining Equations 10 and 11 gives the sediment volume change due to ripple shrinking (sh) during lateral ripple migration (la) ($\Delta\overline{V}_{\text{sh,la}}$), and when divided by the migration time, T, we derive the sediment flux contribution due to shrinking or ripples propagating in the lateral flume direction ($q_{b,\text{sh,la}}$),

$$q_{b,sh,la} = \frac{\Delta\overline{V}_{sh,la}}{T} = \frac{d\left(\frac{1}{2}n\eta\lambda\right)}{dx}LV_{mig,la}. \tag{12}$$

During downslope ripple progression (down) ($\pm y$-direction—across tank), the sediment flux contribution due to ripple shrinking is defined by

$$q_{b,sh,down} = \frac{\Delta\overline{V}_{sh,down}}{T} = \frac{d\overline{V}}{dy}V_{mig,down} = \Delta\left(\frac{1}{2}n\eta\lambda\right)V_{mig,down}. \tag{13}$$

2.6.4. Total Sediment Flux

To estimate the total diffusive sediment flux (sand moving from the top of the mound to the sides and base of the mound), we define a threshold contour on the mound where there is no bed elevation change over the full series (i.e., the threshold between the region of erosion of and the region of accretion on the mound). We can use the contour as a threshold over which we calculate contributions of ripple and gravity driven sediment flux to the diffusion of the sediment mound. All estimates of sediment flux are performed along or through the threshold contour.

To quantify the time ($\bar{\cdot}$) and space ($\langle\cdot\rangle$) integrated sediment flux through the threshold contour contributing to mound diffusion ($\langle\overline{q}_{mound}\rangle$, which is equivalent to the volumetric change of the mound $\Delta\overline{V}_{\text{mound}}$), we time integrate of all of the sediment flux contributions from Equations 5, 9, 12, and 13 along the threshold contour,

$$\Delta\overline{V}_{mound} = \langle\overline{q}_{mound}\rangle = \int_0^{2\pi}\int_{t_a}^{t_b}(q_{b,down} + q_{b,la} + q_{b,sh,down} + q_{b,sh,la} + q_{b,avlch})\,dt\,r(\theta)d\theta \tag{14}$$

where $r(\theta)$ is the distance between the center of the mound and threshold contour with respect to angle around the mound, and the integration is performed through space (from 0 to 2π around the mound) and with respect to time from t_a = time zero to t_b = the end of the series.

3. Results

Prior to showing results of the sediment flux contributing to each measured diffusion process, we show the overall patterns of diffusion of the mound over time. We then show details of each diffusion process and measured hydrodynamic patterns contributing to diffusion of the mound. Finally, we present results that quantify the

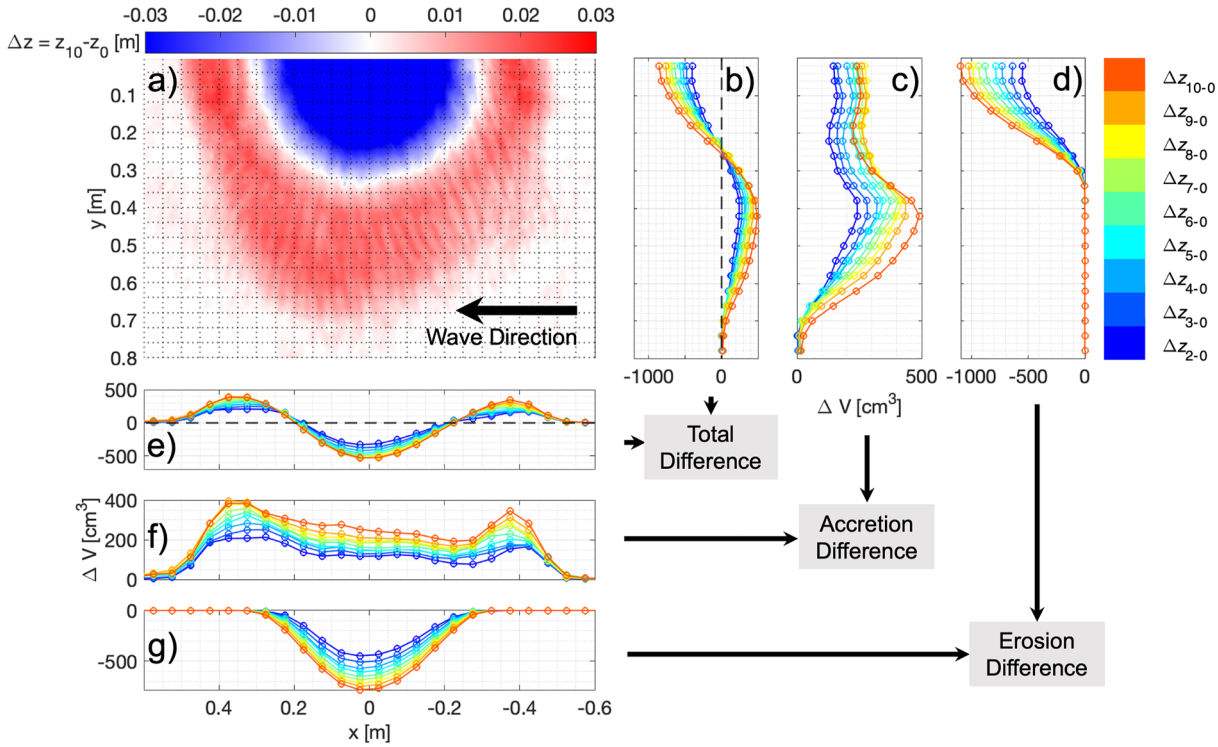

Figure 5. Volumetric change of the sand mound for Series 1. As the mound is symmetrical about the *y* axis, only half of the mound is shown. (a) Elevation change between pre- and post-series lidar scans (red is accretion and blue is erosion). The point between accretion and erosion is defined as the contour around the mound with no change, where accretion of sediment is indicated as positive elevation difference and erosion of sediment is indicated by negative elevation difference. (b and e) Illustrate the volumetric change between each run and the initial mound profile, spatially integrated in the *x* and *y* directions, respectively with $dx = dy = 0.05$ m. (c and f) Show the accretional component of total volumetric change and (d and g) show the erosional component. In (b–g), the difference between runs is indicated as subscript of *z* in color bar.

sediment flux contribution from each ripple and slope driven process leading to mound diffusion as outlined in the Methods section.

3.1. General Patterns of Mound Diffusion

General patterns of sediment deposition and erosion were observed by differencing the pre- and post-series lidar scans and each RPS sonar scan collected after each run during the series (Figure 5).

We show the total morphological difference (Figures 5b and 5e) as the summation of the accretional and erosional difference. We find that the total erosional volume (Figures 5d and 5g) of the mound is balanced by the total accretional volume of sediment moved from the top of the mound and diffused down the mound side slopes (Figures 5c and 5f). The accretional patterns (Figure 5a) show relatively large amounts of sediment are deposited along the *y*-direction side lobes of the mound (Figure 5f) compared to the *x*-direction on the shoreward and wave maker sides of the mound (Figure 5c). We see that the accretional volume in the *y*-direction is spread over a longer length, approximately 40 cm on each side of the mound compared to 20 cm in the *x*-direction on each shoreward and wave maker areas of the mound. Additionally, we observe that there is increased accretion on the shoreward side of the mound (Figure 5e, $x = 0.4$ m, direction of wave propagation) compared to the wave maker side (Figure 5e, $x = -0.4$ m).

We explore basic time and phase averaged hydrodynamic patterns that may contribute to the morphological diffusivity of the mound (Figure 6). Within the first run, the mound diffused rapidly so the wave velocity changed through the 15 min progression at each of the V1–V4 pADV stations (Figures 6a–6c colors). We observe that $\tilde{u}$ are in phase across the sides and downslope of the mound (V1–V4) (Figure 6a) and the largest wave velocities occur near the mound top (V1 and V2). The waves are considered to be in intermediate depth water at the base of the mound (Table 1), so the wave component velocities decay with depth moving down the sides of the mound (V3 and V4). The amplitude of $\tilde{u}$ at V1 and V2 is observed to decrease with time as the mound top erodes, and the

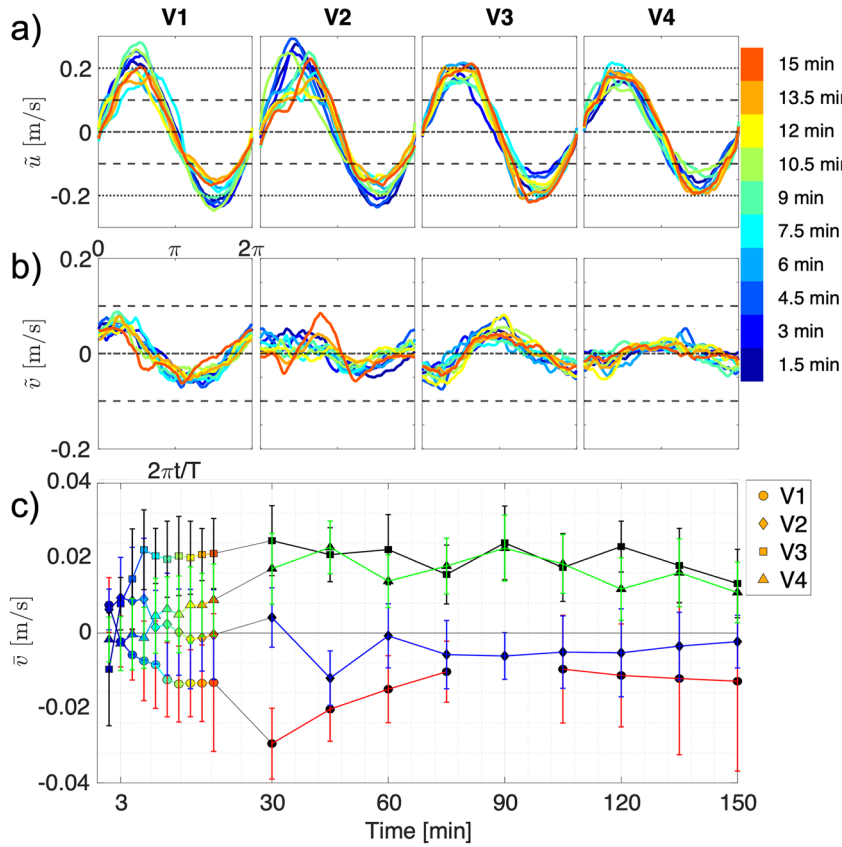

Figure 6. Hydrodynamics forcing across the sand mound. (a) Phase-averaged wave velocity for each Profiling ADVs (pADV) V1–V4 for $\tilde{u}$ and (b) $\tilde{v}$ components. Symbol colors in panels (a–c) correspond to time as shown in the colorbar next to panels (a and b) (only shown for first run). Dash-dot line, dashed line, and dotted line on panels (a and b) are corresponding to the 0, ±0.1, and ±0.2 m/s. (c) Mean current velocity in the *y* direction for each pADV for all runs. Mean current velocity during the first run was estimated for each 90 s (1.5 min) interval, and subsequently all runs for Series 1 are shown as run averaged current velocities (subsequent black filled symbols). Symbol shapes correspond to V1–V4 (same as Figure 3b). ±Standard deviation error bars are placed on each mean current value (red, blue, black, and green correspond to V1, V2, V3, and V4, respectively).

amplitude of $\tilde{u}$ is observed to increase with time as the side lobes of the mound accrete (V3 and V4). Additionally, we observe that $\tilde{v}$ (cross-tank wave velocity) was non-negligible around the mound (Figure 6b), and is attributed to the mound itself creating 3D flow. The *y*-directed wave velocity is non-zero and out of phase between the four positions (V1–V4) (Figure 6b). At V1 (right side of mound) the $\tilde{v}$ component is negative with a phase of approximately 0.5 $2\pi t/T$, at the same phase V3 and V4 (left side of mound) the $\tilde{v}$ component is positive with decreasing amplitude from V3 (middle side) to V4 (base) due to intermediate wave energy conditions. Finally, V2 (top of mound) the $\tilde{v}$ component varied near zero. The patterns in the phase averaged $\tilde{v}$ indicates a cyclic downslope component of the near bed wave velocity along the sides of the mound. We attribute the non-zero $\tilde{v}$ (cross flume wave velocity) to be important for driving downslope currents on the sides of the mound. Velocity skewness and asymmetry were investigated, but there is no significant relation between the wave velocity skewness and asymmetry to ripple processes and the three-dimensional mound diffusion (see Text S2 and Figure S1 in Supporting Information S1 for details).

The time-averaged current velocities $(\overline{v})$ during the initial stages of mound diffusion (Figure 6c colors) show that after 6 min the downslope currents reach quasi-equilibrium and remain consistent for the remainder of the series. Similar to $\tilde{v}$, estimated $\overline{v}$ at each pADV position shows a negative downslope directed current on the mound right (V1), nearly negligible current at the top of the mound (V2), and positive downslope directed current on the mound left (V3 and V4). As such, we observe a downslope directed current on both sides of the mound (*y*-directed current). The magnitude of the downslope current on the middle side of the mound is observed to be nearly 3 cm/s in magnitude, which is approximately 15% of the wave orbital velocity at the

same location. The wave- and morphology-driven currents are considered to be important drivers for gravity driven, downslope ripple progression driven, and lateral ripple driven transports and the resulting mound diffusion.

3.2. Mechanisms of Ripple-Induced Mound Diffusion

Observations of the sediment mound during all stages of diffusion show it to be covered by small ripples (Figures 4a–4d and 5a, see Movie S1 file for more detail). As such we investigate the potential for sediment flux divergences driven by mechanisms of ripple and gravity driven sediment transport to contribute to broader patterns of mound diffusion. The mechanisms we investigate include lateral ripple migration, downslope ripple progression (downslope movement of the ripples in longitudinal direction, form of gravity driven avalanching), sediment avalanching, and ripple shrinking leading to sediment deposition as potential mechanisms contributing to diffusion of the sediment mound. We sub-divide the series as three subsets of runs based on the observations through rectified GoPro images. The first subset (runs 1–3) are downslope ripple progression/gravity driven dominant, the second subset (runs 4–6) transition from downslope/gravity to lateral ripple migration dominant, and the third subset (runs 7–10) are lateral ripple migration dominant. The total sediment volume flux is estimated by integrating the erosional volume of the top of the mound at each time step. Ripple shrinking for the first time step was neglected (Figures 7a and 7b). Uncertainties are estimated for each mean value and are based on the standard deviation of the mean ripple height, migration rate, and ripple wavelength; uncertainty is propagated using standard error methods (see Text S3 in Supporting Information S1 for more detail). In Figure 7 we quantify the volumetric sediment flux attributed to each described mechanism. The dark blue bar to the left of each subset of runs shows the total volumetric flux related to erosion of the top of the mound during each time period (Figure 7b). The right composite bar shows the contribution of each measured sediment flux process contributing to diffusion of the mound as measured through the threshold contour. By comparing the accumulation of each sediment transport process with the volumetric flux of mound top erosion, we nearly close the sediment budget for the mound diffusion. Our observations show that sediment flux driven through ripple and slope driven processes account for the near total volumetric mound diffusion to within 10% of the total mound diffusional volume. These results underline the impact that small scale sediment transport processes can have on larger scale morphological diffusion.

Most volumetric sediment flux due to the mound top erosion is explained by ripple- and slope-driven processes (Figures 7a and 7b). The largest contribution of sediment flux to diffusion for the first subset of runs (runs 1–3) is driven through downslope ripple progression. If we consider mobile layer avalanching as a form of downslope ripple progression, then downslope ripple progression accounts for approximately 85% of the total sediment volume change during runs 1–3. As the slope decreases, the contribution of downslope ripple progression/avalanching decreases during the second and third subset of runs (runs 4–6 and 7–10) to less than 50%. For the second and third subsets, the increase in the contribution of lateral ripple migration suggests that new ripple formation due to continuous ripple splitting increases the sediment transport capacity, which is corroborated by the increased volume change by lateral ripple migration (Figures 7a and 7b). Even though downslope ripple progression is significant for all three subsets of runs (Figures 7a and 7b), we see that the ratio of sediment flux driven through lateral ripple migration to downslope ripple progression and mobile layer avalanching increases from less than 10% for the first three runs to about 40% for the remaining runs (Figure 7c). The initial mound diffusion is dominated by sediment flux driven by downslope ripple progression and avalanching of the mobile layer due to mound slope steepness and gravity (runs 1–3), and as the mound slope decreases due to mound diffusion, the downslope ripple progression and mobile layer avalanching contribute less to the total volumetric sediment flux as measured through the mound top erosion over each run subset. Formed ripples begin to migrate laterally and include changes in their contribution because of their mobility and changing volume from ripple splitting and shrinking (run 4–6 and 7–10). The volumetric sediment flux during the third subset of runs in particular is mostly comprised of sediment flux gradients driving diffusion through the lateral ripple migration mechanism (Figures 7a and 7b). During this period, sediment continues to accrete on the sides of the mound due to sediment flux driven through mobile layer avalanching and ripple shrinking, which moves sediment from the mound top to feed spreading of sediment via the lateral ripple migration mechanism. A mechanistic schematic of mound diffusion driven by sediment flux contributed from various ripple migration and gravity driven processes (Figure 8) shows the changing contributions of each process during the three stages of mound diffusion observed. Following, we present results related to the sediment flux driven through each observed diffusional process.

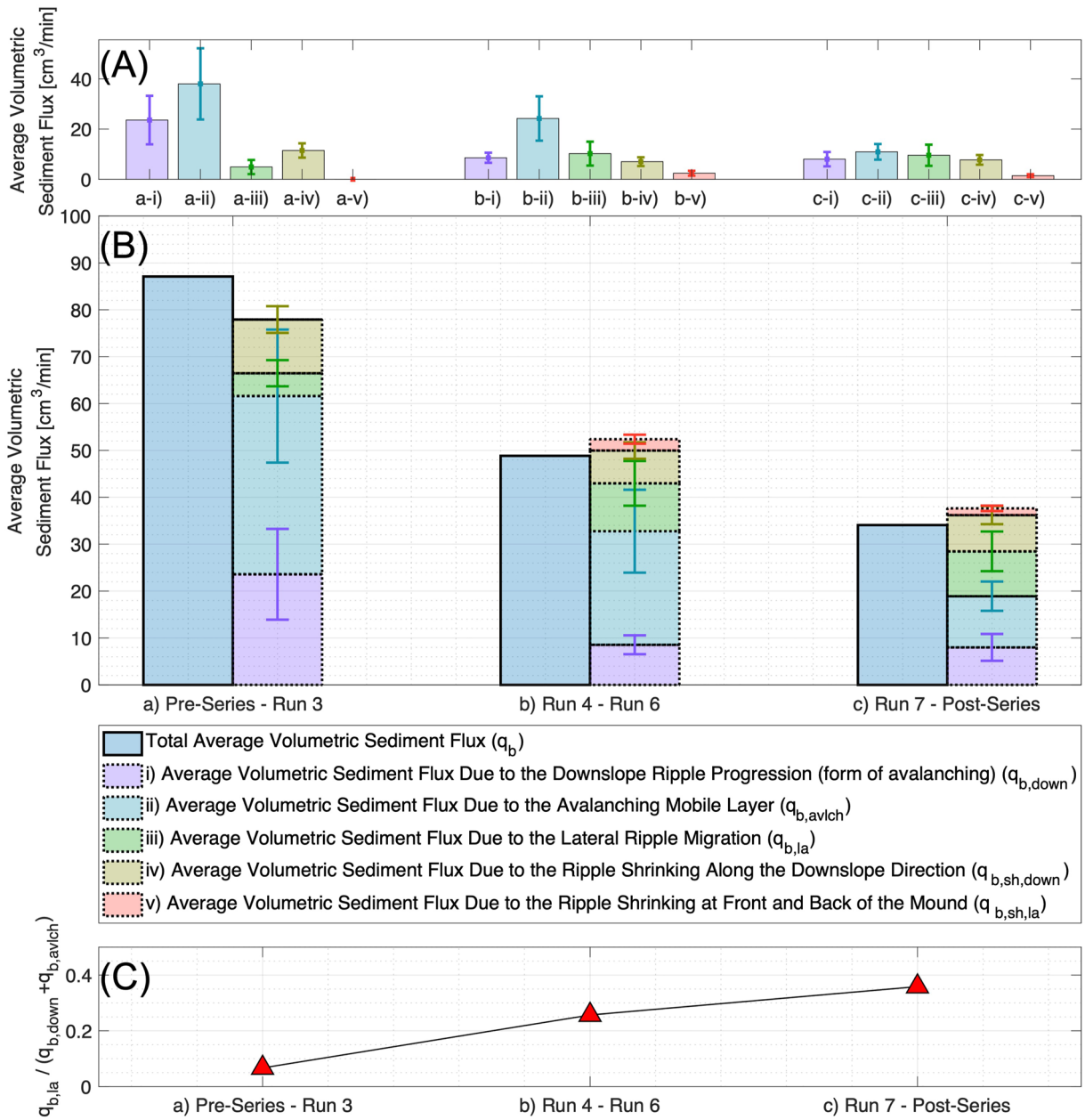

Figure 7. (a) Volumetric sediment flux contributions to mound diffusion as measured through ripple driven sediment transport and gravity driven transport with corresponding uncertainty. See legend below panel (b) for the key to contributions. (b) Total volumetric sediment flux considering packing density for each run subset (shown as dark blue bar to left of each column) and the cumulative volumetric sediment flux contribution during each run subset from each ripple/gravity-driven diffusion mechanism (shown as the colored and stacked bars to the right of each column) with corresponding uncertainties. (c) The relative ratio between sediment flux driven through lateral migration and through downslope ripple progression and mobile layer avalanching for each subset of runs (downslope driven = 0 and lateral driven = 1).

3.2.1. Downslope Ripple Progression

We observed downslope ripple progression as the ripple terminus appears and propagate down the side of the mound (Figures 9a and 9b). Rapid propagation of the ripples toward the *y*-axis side lobe of the mound was observed during the first 10 min of run 1. The yellow tracked line (Figure 9a) follows the path of downslope ripple progression; between 1 and 2 min the terminus of the ripple moves by about 0.2 m in the *y*-direction, or with an approximate 20 cm/min downslope ripple progression rate. However, as time persists, the downslope ripple terminus progression slowed, between 4 and 10 min the terminus of the ripple migrated at a rate of 1.7 cm/min in the *y*-direction. The sediment accretion between $y = 0.4$ and 0.7 m from the top of the mound (Figure 5c)

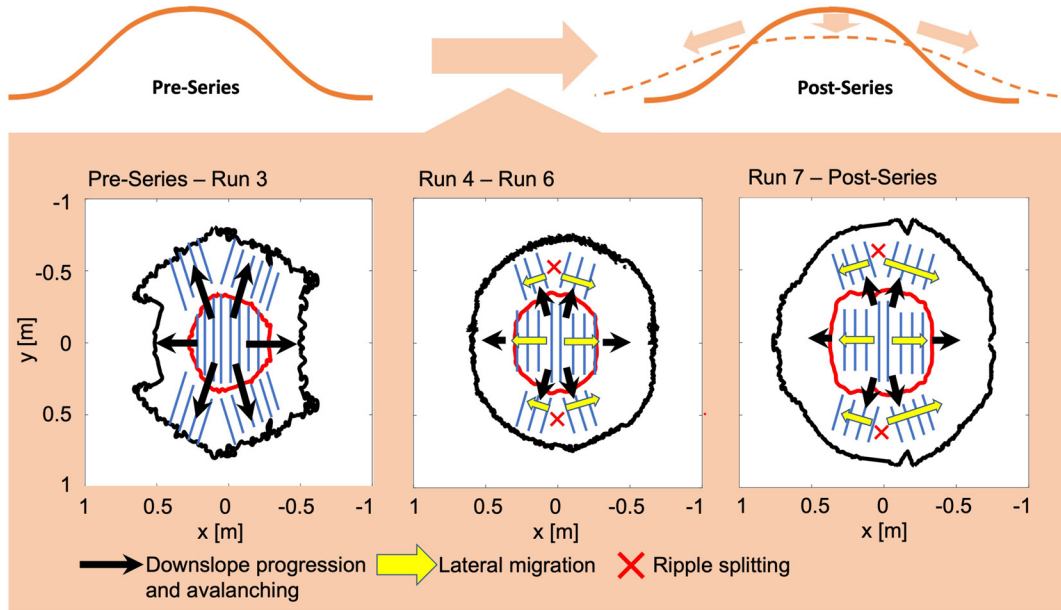

Figure 8. Mechanistic schematic of mound diffusion driven by sediment flux contributed from various ripple migration and gravity driven processes. Top panel shows mound diffusion (decrease in height and increase in diameter). Bottom panel shows mechanistic processes broken down by labeled run subsets. The inner red contour indicates the elevation of the transition from erosion to accretion for each run subset, and the outer black contour indicates the position of the base of the mound at the end of each subset. Downslope ripple progression and avalanching are shown with black arrows, lateral ripple migration is shown as yellow arrows, and red crosses indicate ripple splitting positions.

after run 1 is attributed to downslope ripple progression. Rapid sediment flux driven through downslope ripple progression at the very beginning of the first run was concomitant to observed erosion at the center of the mound, subsequently the sediment flux driven through downslope ripple progression decreases as the slope of the mound became more mild. Once the ripple terminus is observed to approach the pADV, ripple wavelengths remain relatively large (about 5 cm), which is out of equilibrium with the orbital excursion at that elevation and as such indicates that the ripple was formed near the mound top where larger orbital excursions occur. The larger ripple then is forced to progress along the downslope of the mound (Figure 9b), which is a form of mobile layer avalanching.

3.2.2. Mobile Layer Avalanching

The average slope angle and cross-sectional area of ripples along the threshold contour are used to estimate the contribution of mobile layer sediment transport to the volumetric sediment flux through the threshold contour leading to mound diffusion (Figure 8). The mean velocity of the mobile layer avalanching is estimated by Equation 8, and associated erosional volume with uncertainty is shown in Figure 7. Results shows that approximately half of the erosional volume during the first subset (runs 1–3) is associated with mobile layer avalanching, and the contribution of mobile layer avalanching decreases during the subsequent subsets because of the mound slope decay. We assumed the mobile layer to encompass half of the ripple height; however, at steeper slopes, the mobile layer may be thicker, which would increase the contribution of sediment flux due to mobile layer avalanching during the first subset of runs. Mobile layer avalanching of sediment down the sides of the mound uses the sand ripples as a sediment pathway, as such, we cannot differentiate sediment flux driven by avlanching from the influence of ripples on enabling that sediment flux.

3.2.3. Lateral Ripple Migration

After the ripple terminus reaches the base of the mound, the transport mechanism shifts to lateral migration in both the positive and negative x-direction (Figures 8 and 9b). Fairly constant lateral migration rates of 0.08 cm/min observed in the positive x-direction and 0.17 cm/min observed in the negative x-direction, shown by the constant slope of the tracked ripple crest position in the time-stack (between time 150 and 300 in Figure 9b). Both crest lines migrate from the center of the mound ($x = 0$ m in Figure 9b) with newly generated ripples forming near

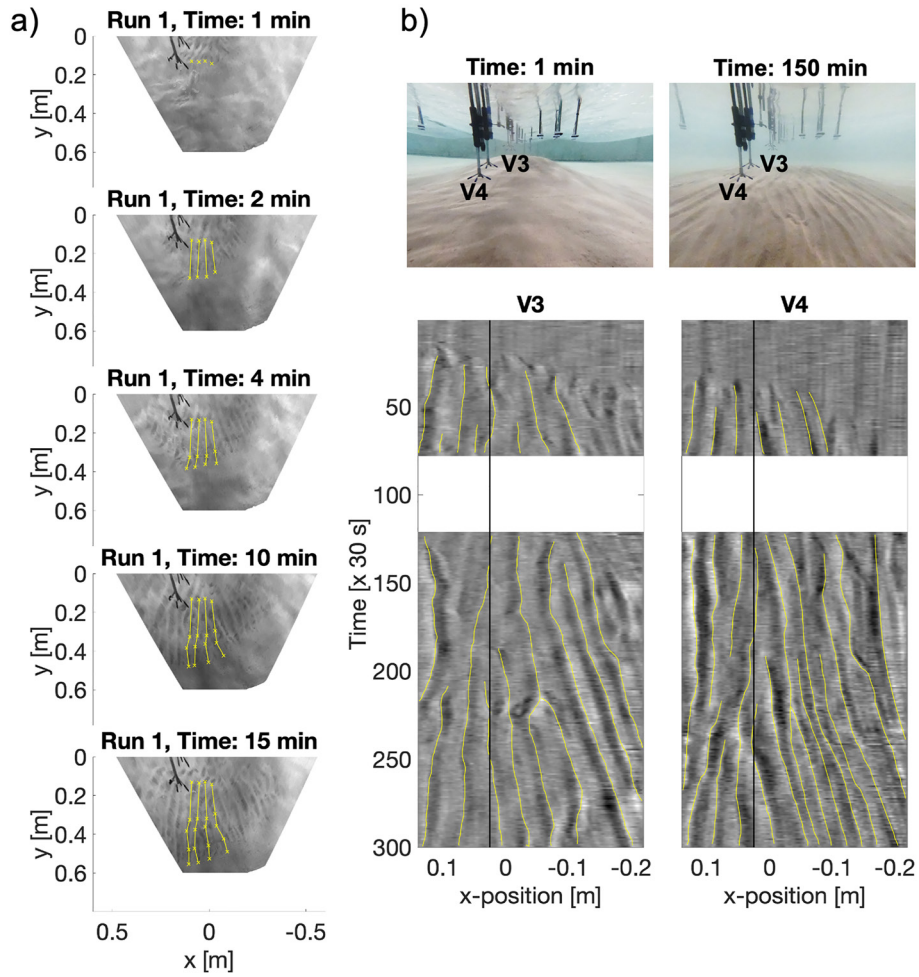

Figure 9. Downslope ripple progression and lateral ripple migration observed during Series 1. (a) Rectified images show downslope ripple progression by tracking of the ripple terminus in yellow, the time is marked at the top of each subpanel. ((b)-top) GoPro images from pre-series to post-series are shown in the two top panels. ((b)-bottom) Time-stack showing the progression of lateral ripple migration at the mound elevation under V3 and V4 showing tracked ripple crests in yellow. Black vertical solid lines show the *x*-location of each Profiling ADVs, white horizontal bands indicate missing data.

the center of the mound, causing pre-existing ripples to continuously migrate laterally in both the $\pm x$ directions (Figure 9b).

The interpolated time evolution contours of the estimated ripple geometry (Figures 10a-i and 10a-ii), lateral migration rates (Figures 10b and 10c), and spatial estimates of ripple volume based on lidar data (Figure 10a-iii) are shown in Figure 10. In Figures 10b and 10c, the panels are broken into three subsets of runs for (i) during dominant downslope ripple progression and weak lateral migration except shoreward and wave maker sides of the mound due to the large initial slope ($0 < y < 0.5$ m, Figures 10b-i and 10c-i), (ii) during shifting dominance to lateral migration with decreasing downslope ripple progression, and (iii) during continuous lateral migration and weak downslope ripple progression.

3.2.4. Balance of Gravity Driven Downslope Ripple Progression and Avalanching With Lateral Ripple Migration

Downslope ripple progression and mobile layer avalanching forced large *y*-directed mound diffusion (across tank), while lateral migration forced sediment spreading in the *x*-direction. Sediment deposited on both the wave maker and shoreward sides of the mound (along the *x*-direction, Figure 5) is primarily caused by lateral ripple migration. The accumulated sediment on the sides of the mound is skewed toward the shoreward side of the mound (positive *x*-direction), in the same direction as wave propagation. We compare diffusion patterns

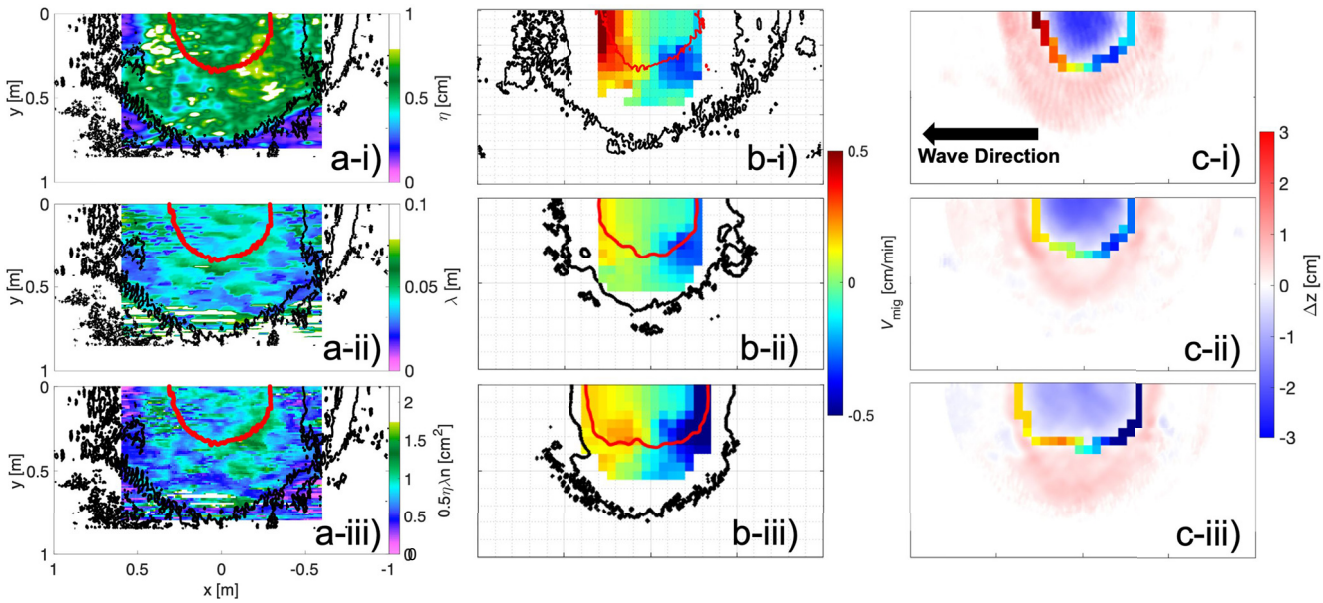

Figure 10. Time evolution of interpolated ripple-induced mound diffusion estimated from downslope ripple progression and lateral ripple migration for Series 1. Only one half of the mound is presented. (a-i–a-iii) Show ripple height, ripple wavelength, and ripple volume, respectively. Red and black contours show erosional contour (inside) and threshold of accretional area (outside), respectively. (b) Interpolated average lateral ripple migration rate (color), inside contour line (red) shows threshold between the erosional (inside) and accretional (black outside) regions of mound, black contours outline the base of the mound. (c) Observed regions of volumetric erosion (blue) and accretion (red); colored contour line shows the lateral migration rate as observed at the erosion threshold contour line (threshold line coloring corresponds to colorscale in panel (b)). Time steps correspond to (i) between pre-series and third run (downslope-directed progression dominant), (ii) between the fourth run and sixth run, and (iii) between the seventh run and post-series (lateral directed migration dominant). The lateral migration rate on the threshold contour is used to estimate the volumetric sediment flux driven by lateral migration through the threshold contour from the central erosional area and diffused to the sides of the mound.

during runs 1–3 (Figure 11a) to runs 4–10 (Figure 11b) to estimate the relative contribution of sediment flux driven through downslope ripple progression and mobile layer avalanching with that of lateral ripple migration to overall mound diffusion. The time interval for Figure 11a is 45 min and Figure 11b is 105 min, during which approximately the same volume of sediment was diffused from the mound top. Diffusion was therefore observed to occur almost two times faster during the beginning of the series (runs 1–3) compared to the middle-end. We hypothesize that the rapid initial downslope ripple progression from the center of the mound (Figure 9a) results in a larger magnitude of downslope sediment flux (Figure 11a). Additionally, the timing of slowing downslope ripple progression (Figure 9a) coincides with lower rates of mound top diffusion (Figure 11b).

During runs 1–3, we found that downslope/gravity driven sediment transport was important to mound diffusion, and after run 3 when the mound slope became more mild, volumetric sediment flux driven by lateral ripple migration seems to become more important for distributing sediment around the mound. To confirm these observations we first determine the ratio (r) of accreted to eroded volume of the mound for runs 1–3 and runs 4–10 (Figure 11c) and then we take the ratio between such quantities $R = r_{4-10}/r_{1-3}$ (Figure 11d), which shows the relative change in normalized accretional volume within each directional sector between the period where we believe downslope sediment flux (runs 1–3) to be more dominant than lateral sediment flux (runs 4–10). A relative ratio, $R > 1$, indicates that the accretion volume ratio during runs 4–10 > accretion volume ratio during runs 1–3. The accretion patterns indicate a greater lateral directed mound diffusion along the $\pm x$-direction of the mound during the middle-end runs 4–10 (Figure 11b) compared to the beginning runs 1–3 (Figure 11a). We observe $R > 1$ (red) near the shoreward and wave maker sides of the mound (e.g., at −45° and +45°). The $R < 1$ values (blue) on the sides of the mound (0°) indicate that more sand was deposited during runs 1–3 than during runs 4–10 on the sides of the mound, where we observed downslope sediment flux to be important. We deduce that the relatively large accretional volume at the side of the mound is due to downslope ripple progression and subsequently the accreted sediment from downslope ripple progression diffuses in the $\pm x$-direction due to lateral ripple migration.

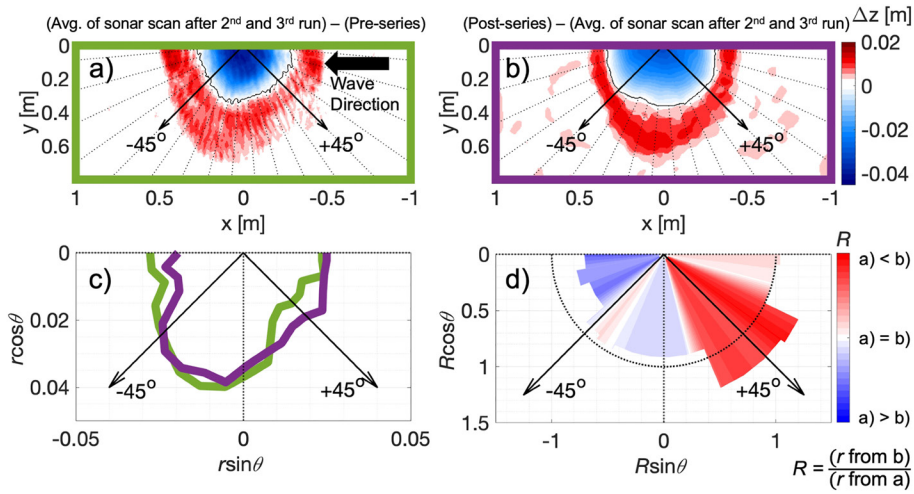

Figure 11. Sediment volume change during Series 1 for two representative time intervals. Only one half of the mound is presented. Wave direction is from right to left (positive *x*-direction). (a) Bed level change between pre-lidar scan and average of sonar after run 2 and run 3; downslope ripple progression is dominant. (b) Bed level change between post-lidar scan and the average of sonar scans after run 2 and run 3, lateral migration is dominant. (c) The domain of panels (a and b) are divided into 10-degree sectors, shown by dotted lines. The $r = \overline{V}_k / \overline{V}_{\text{total}}$ is the ratio of the accretional volume in each sector to the total eroded volume of each subset of runs. *r* Is calculated and plotted in panel (c), for panel (a)-green and panel (b)-purple. (d) Relative accretion ratio, $R = r_b/r_a$, between panel (a) and panel (b), when $R > 1$, the sector in panel (b) has relatively more accretion than that sector in panel (a).

3.2.5. Ripple Splitting

During lateral migration, new ripples form through the mechanism of ripple splitting, where sediment is deposited in-between two large ripples at the center of the mound. Figure 12 shows low-pass filtered observations of ripple wavelength extracted from wavelet analysis at the mound elevation associated with V3 for Series 1.

Based on the time-stack of ripple wavelength growth and shrinking estimated using wavelet analysis at a mound elevation under V3 (Figure 12) and a corresponding time-stack image (Figure 9) we track four representative ripple splitting events. The waterfall plot shows ripple splitting events marked with a diamond at times 149, 182, 206, and 242 (Figure 12b). The ripple wavelength decreases when ripple splitting occurs, and thereafter, the ripple wavelength again begins to lengthen. All of d_0/D values from the MODEX experiment were in a narrow band, as the wave orbital diameter was not measured to vary significantly over the mound (see Text S4, Figure S2, and Figure S3 in Supporting Information S1 for more detail), and we observe the ripple wavelength to grow with time before abruptly decreasing in size near the splitting points (Figure 12b). Therefore, during ripple splitting events, we see that the ripple wavelength is independent of the wave orbital diameter, which suggests that waves alone are not solely responsible for driving ripple growth and splitting cycles. Ripple growth is instead modified by mound bathymetry, gravity, and the wave-driven current, which continuously force sediments from the top of the mound down the slope. The central ripple acts as a pathway for sediments at the top of the mound to diffuse to the bottom of the mound. As such, the central ripple does not scale with the wave orbital diameter during periods of ripple growth. Although we cannot visually see the continuous movement of sediments parallel to the ripple crests once the initial downslope ripple progression period ends, the constant growth and splitting cycles of the central ripples on the mound indicate that sediments are continuously being transported downslope during the experiment. Interestingly, during ripple growth, we observe the ripple maximum wavelength to reach the normalized ripple wavelength of anorbital ripples in Clifton and Dingler (1984), but at a much smaller normalized wave orbital diameter than previously observed anorbital ripples in Clifton and Dingler (1984). Additionally, prior to ripple growth and after ripple splitting, the ripple scaling returns to the wave orbital ripple regime. When ripple splitting occurs, the larger ripple at the center of the mound that was created by downslope flow of mound top sediment is the source for newly generated ripples with smaller ripple wavelengths (see Text S4, Figure S2, and Figure S3 in Supporting Information S1). The cyclic central ripple growth and splitting is a mechanism for lateral ripple migration which drives lateral volumetric sediment flux on the sides of the mound.

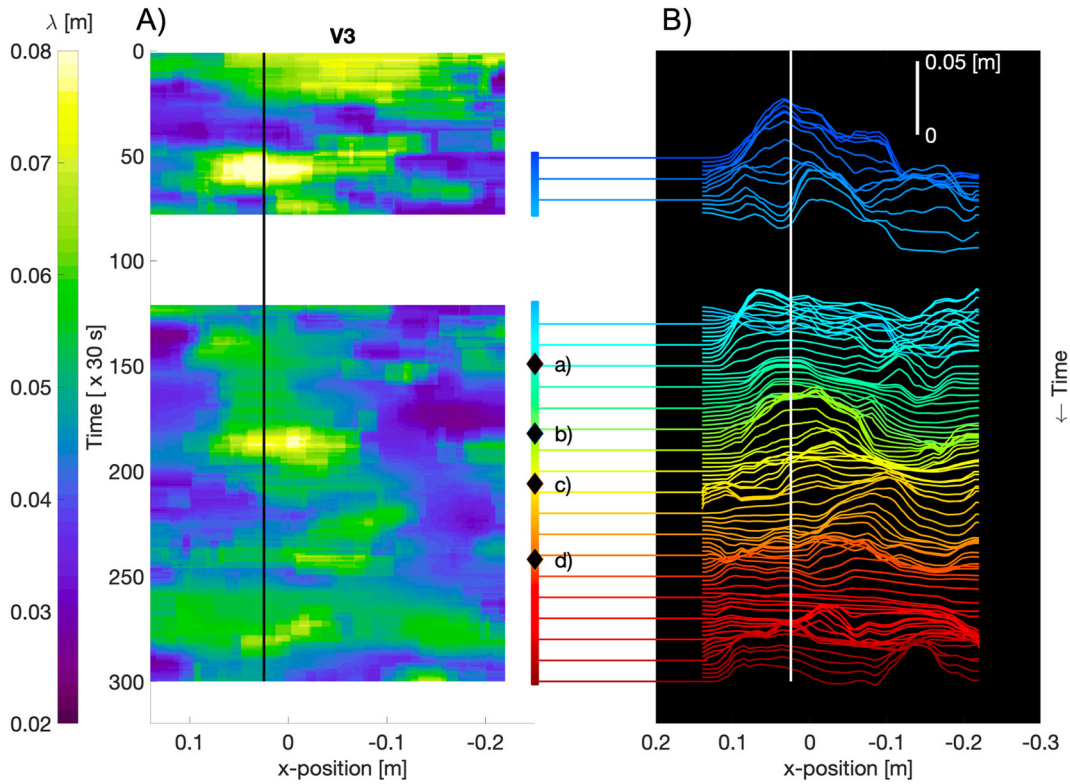

Figure 12. (a) Ripple wavelength variations under V3 extracted through wavelet analysis highlighting ripple splitting and growth events during Series 1. (b) Representative splitting events are illustrated with diamond shape markers at panels (a–d) on the colorbar that illustrates time (from blue to red). Scale bar represents ripple wavelength change with respect to time and *x*-position. Solid vertical lines (black in (a) and white in (b)) indicate the *x*-position of V3. $x = 0$ m is the center of the mound.

3.2.6. Ripple Shrinking

During downslope ripple progression and lateral ripple migration, sediments that constitute the ripple are transported by ripple migration and spread down and around the mound. The ripple geometry also changes from the top to the bottom of the mound (Figures 5a and 10a). Ripple height in Figures 10a-i and ripple wavelength in Figures 10a-ii are used to calculate ripple volume ($0.5n\eta\lambda$) in Figures 10a-iii.

We do not have sufficient data to determine whether ripple shrinking was time-dependent. However, evidence of ripple shrinking is visible in the post-experiment lidar scan data (see Figure 10a-iii). The ripple geometry changes as the ripple migrates farther from the mound top, and presumably during downslope ripple progression. As the volume of the ripples decrease, the ripples deposit excess sand on the sides of the mound. During ripple migration, ripples enter deeper water, in intermediate wave conditions the wave orbital diameter decreases, which drives a reduction in oscillatory ripple geometry. Observations show that ripples shrink in volume by approximately 10%–15% (see Section 2.6 for volume loss estimation and Figure 7). The deposited sediment due to ripple shrinking is a small source of volumetric sediment flux through the threshold contour leading to mound diffusion.

3.3. Observations of Mound Diffusion During a More Energetic Wave Energy Condition

Higher wave energy (Series 2) results in a larger sediment flux contributing to mound diffusion. Unfortunately, the sonar scan data extent did not capture the full window of the mound diffusional area for the more energetic wave condition (Series 2, see Figure 13a), so it is difficult to close the sediment budget as we did for Series 1. However, during Series 2, similar patterns of sediment accretion and erosion were observed (Figures 5 and 13), with the magnitude of sediment diffusion greater than during Series 1.

In Series 2 the erosional area was larger in both volume and diameter than the lower energy case (Series 1) and the accretional lobes were also wider for the higher energy case. Presumably, during the more energetic wave

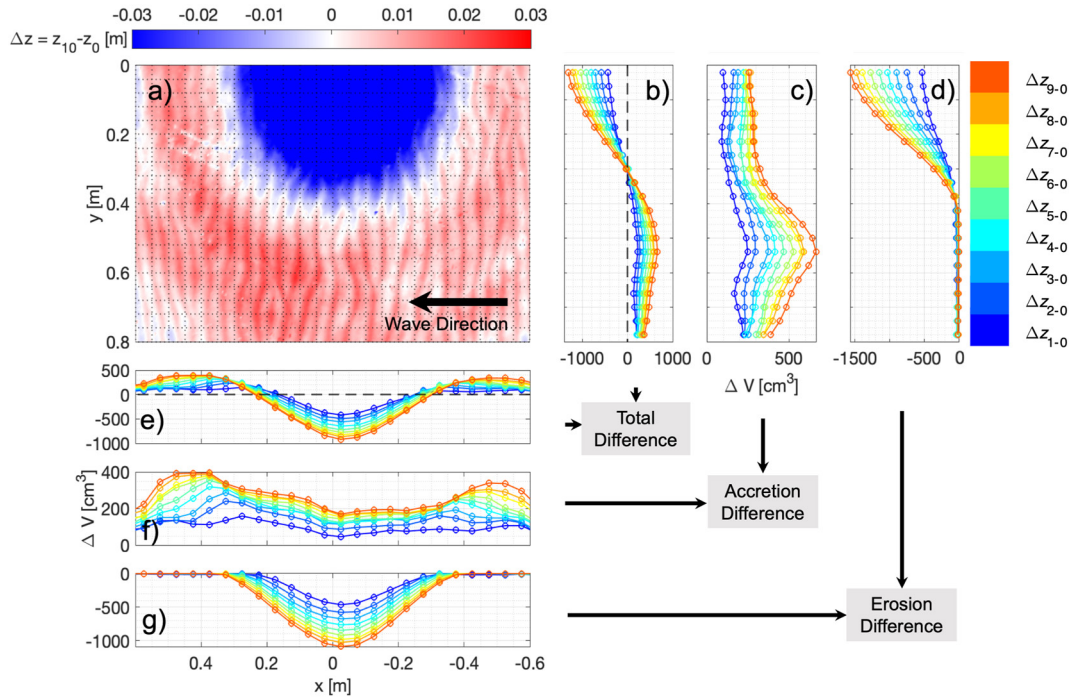

Figure 13. Volumetric change of sand mound for Series 2. (a) Elevation change between pre- and post-series lidar scans (red is accretion and blue is erosion). (b, e) Illustrate the volumetric change between each run and the initial mound profile, spatially integrated in the *x* and *y* directions, respectively. (c, f) Show the accretional component of total volumetric change and (d, g) show erosional component. In panels (b–g) differences in runs are indicated by subscripts to Δz in the colorbar.

condition, the ripples either propagate downslope toward the sides of the mound much faster than during the less energetic wave condition, or it could be that downslope progression of ripples does not occur during the more energetic wave condition because the wave condition invokes shallow water waves at the bottom of the mound, where during Series 1 the wave condition at the bottom of the mound was intermediate. As such, during Series 2, ripples could have formed at the bottom of the mound due to wave orbital forcing rather than formed due to downslope progression from the mound top. In either scenario, the ripples become pathways for sediment avalanching, which causes persistent downslope sediment flux over the duration of the trial.

We observe that the larger volume of mound diffusion during Series 2 results from increased lateral ripple migration rates (Figure 14). However, the increased mound diffusion is also largely affected by larger wave forcing causing greater sediment flux due to avalanching. The top of the mound diffused very rapidly upon the onset of the higher wave energy condition. Consequently, lateral ripple migration, which began after the initial downslope ripple progression during Series 1, occurs almost immediately in Series 2.

With respect to ripple splitting events (Figures 14 and 15), there were fewer splitting instances during Series 2 compared with Series 1. Presumably the more energetic waves drive larger wave orbital diameter ripples, such that the ripple wavelength could support more downslope sediment flux before splitting, causing less frequent ripple splitting events.

4. Discussion

4.1. Significance of Three-Dimensionality of Ripple Process and Implications for Sediment Transport Modeling

The MODEX experiments show that ripple migration and slope driven sediment flux are crucial contributors to three-dimensional mound diffusion under wave forcing, with slope driven flux actually using ripples as the sediment transport pathway down the sides of the mound. The case investigated in the presented manuscript was for non-breaking waves, and we present (to the best of our knowledge) the only study in literature that mechanistically nearly closes the sediment budget for morphologic evolution. In our study, even under monochromatic

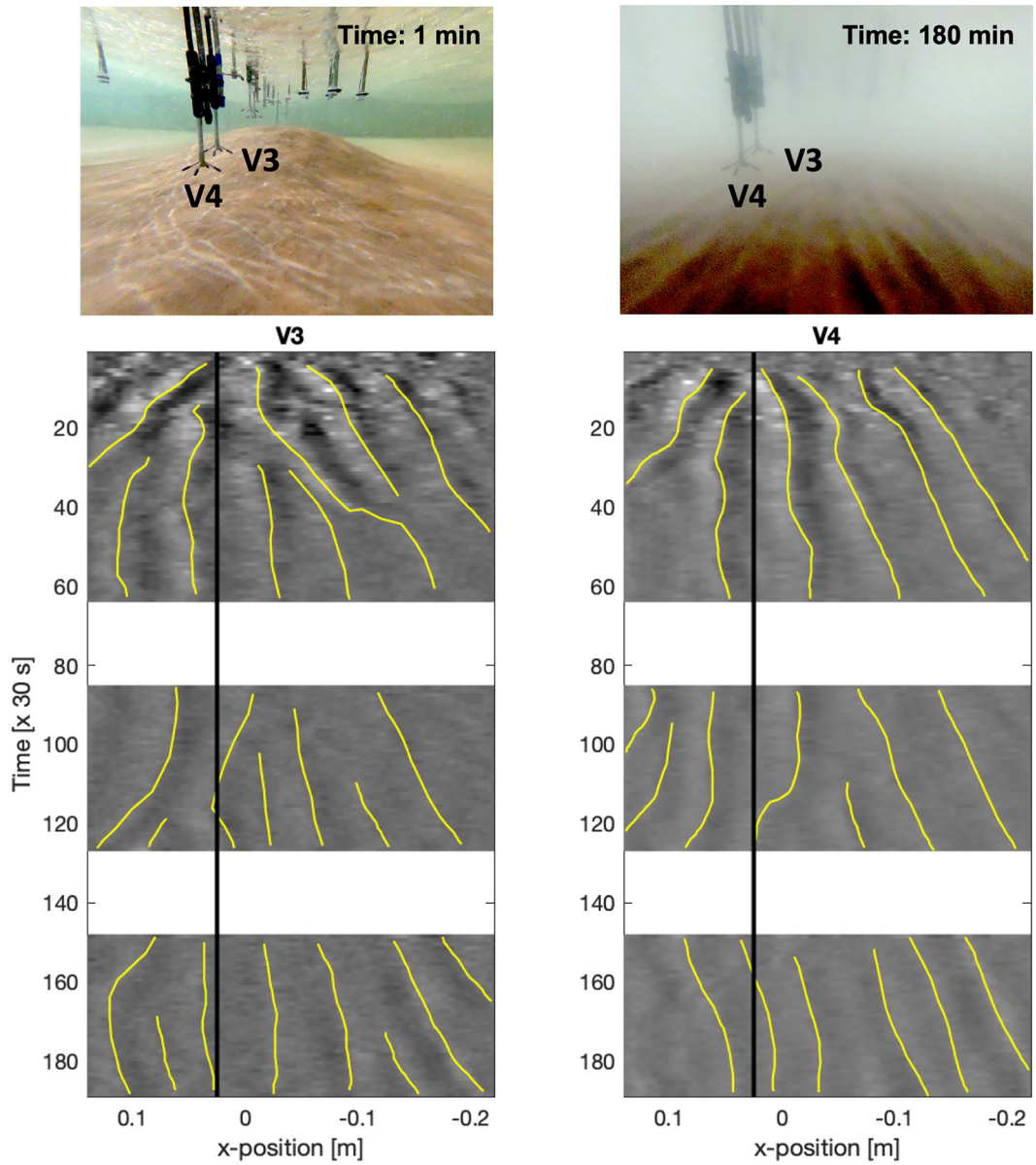

Figure 14. Lateral ripple migration from Series 2 ($H = 0.14$ m, $T = 1.2$ s). GoPro images from pre-series and post-series (top). Bottom: Time-stack at mound elevation under V3 and V4, yellow lines track ripple crests. Black vertical solid lines illustrate x-location of Profiling ADVs V3 and V4, respectively. White horizontal bands indicate missing data.

waves, complex ripple geometry and migration processes over the sediment mound were observed. The three-dimensionality of the sand mound drives three-dimensional hydrodynamics around the mound, which causes mound diffusion due to an aggregation of non-stationary and non-uniform sediment transport processes. We observed that morphology-generated currents had substantial influence over sediment avalanching mechanics, where volumetric sediment flux due to downslope sediment transport/avalanching contributed significantly (30%–70%, dependant on mound slope) to mound diffusion, and lateral migration forced volumetric sediment flux of the majority of the remainder observed. Also, at the wave maker and shoreward sides of the mound, ripple migration rates depend on the mound slope (Figure 16), which show similar trends to existing observations of ripple migration on sloped bathymetries collected in larger scale oscillatory tunnel experiments (Wang & Yuan, 2018).

In order to estimate sediment fluxes, most three-dimensional morphologic change models implement empirical or stochastic shear based sediment transport formulations. Many of the prominent sediment transport

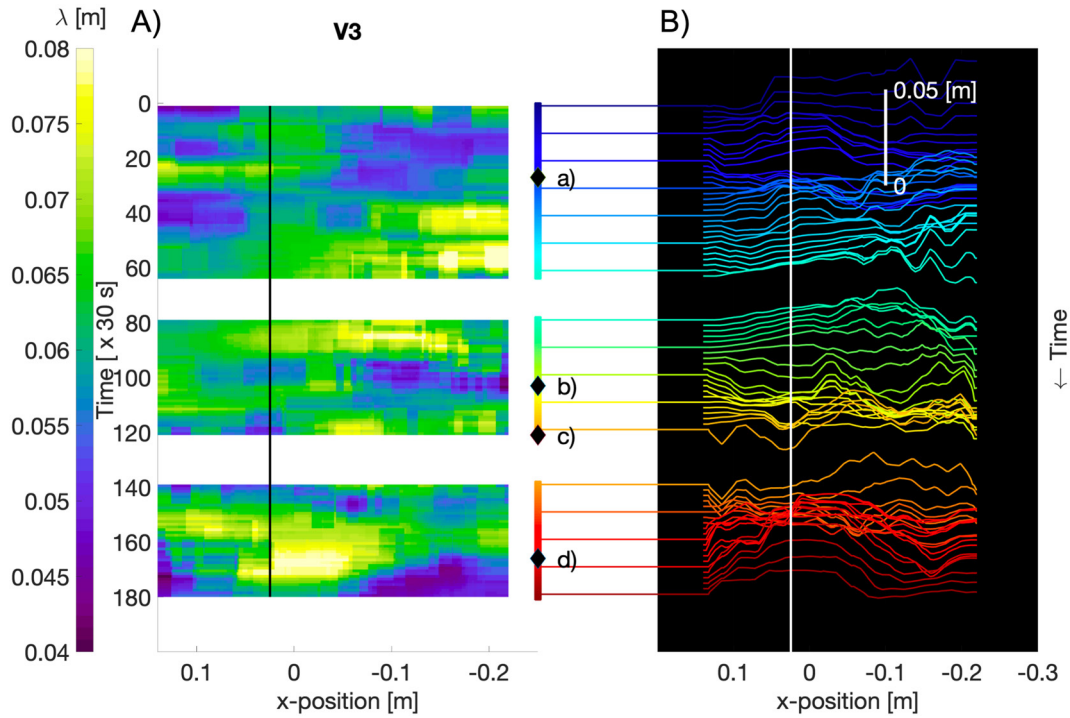

Figure 15. (a) Ripple wavelength variations under V3 calculated using wavelet analysis showing ripple growth and splitting during Series 2. (b) Waterfall plot of ripple wavelength changing in time. Representative splitting events are illustrated with diamond shape markers at panels (a–d) on the colorbar that illustrates time (from blue to red). Scale bar represents ripple wavelength change with respect to time and *x*-position. Solid vertical lines (black in (a) and white in (b)) indicate the *x*-position of V3. $x = 0$ m is the center of the mound.

formulations do not fully capture ripple mechanics nor slope effects in their formulations (Baar et al., 2018; Wengrove et al., 2019). Once sediment transport is calculated, morphologic change is generally modeled using the sediment continuity equation to distribute sediment in the coastal zone (Ancey, 2020). However, current methods for prediction of morphological evolution estimate transport at best within a factor of 2 (Ancey, 2020; Baar et al., 2018; Bosboom et al., 2014; Brakenhoff et al., 2020), which raises the question of how well the transport gradients, that drive morphological change, are modeled around large topographic gradients, such as a mound. Ranasinghe (2020) calls for the need of coastal process based models that incorporate the physics of multi- and intra-scale morphological change. Both dynamic bottom roughness and bed slope effects may need to be more precisely represented in our current suite of morphologic change models to quantify morphodynamic change with greater skill.

Even though the sediment continuity equation (Exner) is theoretically correct, in order to accurately predict morphologic change the sediment flux cannot be assumed to occur uniformly over time and space (Ancey, 2020). Some recent studies suggest an advection-diffusion approach (more representative of gradients in time and space) to modeling sediment flux and morphologic change instead of the sediment continuity approach (Ancey, 2020). Our observations (as with many) are not suited to an advection-diffusion approach because we were unable to observe transport on a grain-by-grain scale. Instead, the three-dimensional ripple and gravity-driven sediment flux process contributions were quantified individually. The variability in space and time of the measured volumetric sediment flux through the threshold contour accounts for the volumetric mound diffusion with high accuracy (Equation 14). With this approach, we were able to nearly close the sediment budget for the diffusion of the idealized mound under highly three-dimensional conditions. While a stochastic grain-scale approach is perhaps not needed, the three-dimensional coverage certainly was.

Hence, morphologic change models should consider all individual transport pathways rather than average estimates of sand fluxes under bulk bedload transport formulations to be better suited to mimic naturally observed three-dimensional morphologic change. Ripple processes generally occur on a sub-grid scale, meaning that

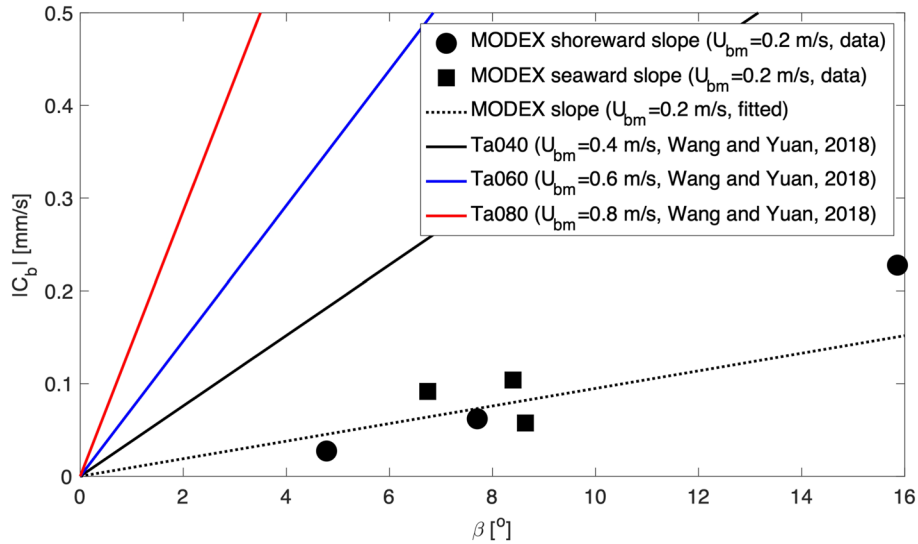

Figure 16. Ripple migration rate (C_b) for different bottom slopes (β). MOrphological Diffusivity EXperiment observations of the shoreward (circle) and wave maker (square) side of the mound during three subsets with different bed slope (same time periods as Figures 8 and 10) are shown by the black markers and black dotted regression line ($U_{bm} = 0.2$ m/s). The black, blue, and red solid lines show regression fits between ripple migration rate and bed slope for larger wave velocity amplitudes (Ta040, Ta060, and Ta080 with $U_{bm} = 0.4$, 0.6, and 0.8 m/s, respectively) observed in Wang and Yuan (2018).

three-dimensional morphodynamic change models generally have grid sizes that are larger than the scale of potential roughness source such as ripples, as such, ripple processes are not modeled directly. This is problematic, because a reduction in grid size for process based models could drastically increase model computation time, and therefore is not realistic. Instead we propose to update sediment transport parameterizations to include ripple-driven transport and the effect of slope. The following are recommendations for improving morphodynamic change models; each recommendation is suggested based on our observations. We suggest to:

1. parameterize a dynamic and non-spatially uniform bed roughness and diffusion coefficient based on wave orbital and mean current conditions as well as on bed slope. We observed ripples to grow or split out of equilibrium depending on the slope of the underlying morphology. The implication is that ripple dimensions and dynamics must be well understood and predictable for the relevant conditions, and particularly for sloping beds, while present ripple predictors are mainly derived from (quasi-)plane bed observations.
2. parameterize the mobile layer thickness and the influence of agitation and gravity on mobile layer avalanching. While the mobile layer may not be as important on flat bathymetries, our observations show that even for mild bed slopes, the mobile layer influences sediment avalanching down the sides of the mound slope. One implication is that this parameterization must be coupled to the sheet flow parameterization, again requiring better understanding of this bed state on sloping beds. The model used herein by Allen (1970), seemed to represent slope driven transport well with a good estimate of mobile layer thickness.
3. represent secondary flows. We observed that secondary flows due to wave and morphologic driven currents had influence on both downslope ripple progression and lateral ripple migration.
4. represent morphology driven transport. We observed that the majority of lateral ripple migration on the mound was only secondarily driven by hydrodynamic patterns; oversized ripples and subsequent ripple splitting to accommodate equilibrium conditions at one place on the mound caused ripple migration to accommodate space for the influx of new sediments on the mound center. As such, ripple migration was not driven by asymmetric or skewed waves, but rather by accommodating for space when ripples adjusted to equilibrium conditions.

4.2. Influence of Scale

The flume-scale experiments are significantly smaller scale than field scale. We cannot actually interpret the small-scale mound diffusion experiment as representative of field scale because of the difference in the length-scale of ripples, neglecting suspended sediment, breaking waves, non-homogeneous sediments, and more.

Consequently, the magnitude of contribution to morphological diffusion in the field may not be completely represented by ripple migration and slope driven sediment flux, as they are in this lab experiment. On the other hand, most sediment transport models that we use in morphologic change models were derived from, or calibrated on, experimental laboratory data. The key variable that we can compare regardless of scale is sediment mobility, which is captured in the laboratory experiments. Rather than being representative for a specific situation in nature, the present experiments serve to identify important processes related to three-dimensional diffusion, where most sediment transport parameterizations were formulated from two-dimensional experiments. We focus on the combination of ripple driven influence and bed slope influence on sediment transport in three dimensional, wave driven flows. As such, the major contribution of our experiments is that they quantify the influence of both ripple migration driven and slope driven sediment flux on three-dimensional bathymetry under waves, which also causes three dimensional circulation. Processes occurring on the field scale may be different in magnitude; however, we can take lessons learned from the laboratory scale into account while considering ways in which we can improve the predictional capability of our morphologic change models. Several recent publications present results from field experiments highlight the potential importance of ripples to larger scale sediment flux (Aagaard et al., 2001; Jones & Traykovski, 2019; Wengrove et al., 2018, 2022), and other larger-scale laboratory experiments have shown the importance of slope driven transport to larger scale sediment flux (Baar et al., 2018; Wang & Yuan, 2018). With our observations, we were able to close the sediment budget over a three dimensional bathymetry, which is no simple feat, and in actuality makes this data set extremely valuable for model improvement (following the suggestions made in the previous section) and model calibration.

5. Conclusions

We present, for the first time, an essentially closed sediment budget for three-dimensional mound diffusion under waves. We show volumetric sediment flux contributions due to four main ripple migration and slope driven processes that sum to account for the total volumetric erosion of the mound top. As such, we show the importance of small-scale sediment transport processes to the large-scale morphodynamic change of a sediment mound.

During both mild and more energetic wave conditions (i.e., Series 1 and 2), our results suggest that sediment flux driven through downslope ripple progression (downslope movement of the ripples in longitudinal direction: $\pm y$-direction) and mobile layer avalanching are the main drivers of the initial rapid mound diffusion when the mound was steep. While Series 1 intermediate water depth conditions forced initial downslope progression of ripples generated on the top of the mound toward the mound base, the more energetic wave forcing of Series 2 caused ripples to form ubiquitously due to shallow water wave conditions at the mound top and base. However, both Series were significantly influenced by mobile layer avalanching of sediments from the mound top to base. Sediment avalanching, which used ripples themselves as sediment pathways, persisted through a combination of both a steep mound slope and strong wave- and morphology-driven currents that forced sediments down the sides of the mound. During this stage, sediment flux due to ripple migration distributed sediment around the mound.

As the mound slope decreased, the contribution of downslope ripple progression and mobile layer avalanching to the total volumetric sediment flux decreased, and ripples on the mound formed during downslope progression started to migrate laterally around the mound (shoreward and wave maker directions: $\pm x$-direction). During both Series 1 and Series 2, lateral ripple migration is the main mechanism of spreading sediments that accumulate near the mound sides and base as a result of downslope ripple progression and avalanching. During lateral migration, new ripples generated from the center of the mound due to ripple splitting. Concurrent with lateral ripple migration, ripple splitting and shrinking further contribute volumetric sediment flux to mound outward diffusion. Ripple splitting occurs from a continuous sediment flux from the top of the mound toward its base that forms large wavelength ripples that act as a primary downslope sediment pathway at the center of the mound; large ripples eventually grow out of equilibrium with the wave orbital diameter and thus split. Ripple splitting drives lateral ripple migration in both the $\pm x$ directions along the mound. During Series 1, we observed more common ripple splitting events because the wave orbital diameter could only support smaller wavelength ripples, while during Series 2 ripple splitting events were less common because the large central ripple could stay in equilibrium with the more energetic wave conditions for a longer period of time. Finally, change in ripple geometry, in this case, ripple shrinking, is the smallest but still noticeable contributor to mound diffusion for both wave energy conditions.

We suggest that a modified approach to sub-grid sediment flux parameterizations be taken, which accounts for the actual contributions of convergence/divergence of flow fields (around three-dimensional bathymetry) and

bathymetric slope on sediment flux and thereby estimates of morphologic change. Our results support that the sediment continuity equation used to propagate morphologic change could be an appropriate approach; however, the simplistic empirical and stochastic sediment transport formulations used to estimate sediment flux may not be robust enough to mimic sediment fluxes in/on complex three-dimensional flows/bathymetries. If sediment flux parameterizations can accurately account for the influence of slope and flow convergence/divergence on sediment transport, the sediment continuity equation may be a reasonable approach to modeling morphologic change.

Data Availability Statement

The processed data used in the study (Two wave-only conditions of MODEX experiment) are available at DesignSafe-CI Data Depot (see Lee et al. (2022), https://doi.org/10.17603/ds2-qzkn-7a92).

Acknowledgments
The MODEX project was supported by the European Community's Horizon 2020 Programme through the grant to the budget of the Integrated Infrastructure Initiative Hydralab+, Contract 654110. We thank the University of Hull Hydralab + Total Environment Simulator staff, including Stewart McLelland, Brendan Murphy, Hannah Williams, and Laura Jordan for their guidance during experiment setup and testing. We also thank the PADI Foundation (project code 11310) for partial funding of participation in the experiments for S-BL and MW. MdS and JH were financed by the Dutch NWO Domain Applied and Engineering Sciences under project code 15058.

References

Aagaard, T., Black, K. P., & Greenwood, B. (2002). Cross-shore suspended sediment transport in the surf zone: A field-based parameterization. *Marine Geology*, *185*(3–4), 283–302. https://doi.org/10.1016/S0025-3227(02)00193-7

Aagaard, T., Davidson-Arnott, R., Greenwood, B., & Nielsen, J. (2004). Sediment supply from shoreface to dunes: Linking sediment transport measurements and long-term morphological evolution. *Geomorphology*, *60*(1–2), 205–224. https://doi.org/10.1016/j.geomorph.2003.08.002

Aagaard, T., Greenwood, B., & Nielsen, J. (2001). Bed level changes and megaripple migration on a barred beach. *Journal of Coastal Research*, 110–116. Retrieved from https://www.jstor.org/stable/25736279

Allen, J. R. L. (1970). *Physical processes of sedimentation*. American Elsevier Pub. Co.

Allen, J. R. L. (1973). Features of cross-stratified units due to random and other changes in bed forms. *Sedimentology*, *20*(2), 189–202. https://doi.org/10.1111/j.1365-3091.1973.tb02044.x

Allen, J. R. L. (1976). Computational models for dune time-lag: General ideas, difficulties, and early results. *Sedimentary Geology*, *15*(1), 1–53. https://doi.org/10.1016/0037-0738(76)90020-8

Allen, J. R. L., & Collinson, J. D. (1974). The superimposition and classification of dunes formed by unidirectional aqueous flows. *Sedimentary Geology*, *12*(3), 169–178. https://doi.org/10.1016/0037-0738(74)90008-6

Ancey, C. (2020). Bedload transport: A walk between randomness and determinism. Part 1. The state of the art. *Journal of Hydraulic Research*, *58*(1), 1–17. https://doi.org/10.1080/00221686.2019.1702594

Baar, A. W., de Smit, J., Uijttewaal, W. S. J., & Kleinhans, M. G. (2018). Sediment transport of fine sand to fine gravel on transverse bed slopes in rotating annular flume experiments. *Water Resources Research*, *54*(1), 19–45. https://doi.org/10.1002/2017WR020604

Baas, J. H. (1994). A flume study on the development and equilibrium morphology of current ripples in very fine sand. *Sedimentology*, *41*(2), 185–209. https://doi.org/10.1111/j.1365-3091.1994.tb01400.x

Bagnold, R. A. (1954). Experiments on a gravity-free dispersion of large solid spheres in a Newtonian fluid under shear. *Proceedings of the Royal Society of London. Series A. Mathematical and Physical Sciences*, *225*(1160), 49–63. https://doi.org/10.1098/rspa.1954.0186

Baldock, T., & Simmonds, D. (1999). Separation of incident and reflected waves over sloping bathymetry. *Coastal Engineering*, *38*(3), 167–176. https://doi.org/10.1016/S0378-3839(99)00046-0

Bosboom, J., Reniers, A. J. H. M., & Luijendijk, A. P. (2014). On the perception of morphodynamic model skill. *Coastal Engineering*, *94*, 112–125. https://doi.org/10.1016/j.coastaleng.2014.08.008

Brakenhoff, L., Schrijvershof, R., Van Der Werf, J., Grasmeijer, B., Ruessink, G., & Van Der Vegt, M. (2020). From ripples to large-scale sand transport: The effects of bedform-related roughness on hydrodynamics and sediment transport patterns in delft3d. *Journal of Marine Science and Engineering*, *8*(11), 892. https://doi.org/10.3390/jmse8110892

Cataño-Lopera, Y. A., Abad, J. D., & García, M. H. (2009). Characterization of bedform morphology generated under combined flows and currents using wavelet analysis. *Ocean Engineering*, *36*(9–10), 617–632. https://doi.org/10.1016/j.oceaneng.2009.01.014

Clifton, H. E., & Dingler, J. R. (1984). Wave-formed structures and paleoenvironmental reconstruction. *Marine Geology*, *60*(1–4), 165–198. https://doi.org/10.1016/0025-3227(84)90149-X

Coco, G., & Murray, A. B. (2007). Patterns in the sand: From forcing templates to self-organization. *Geomorphology*, *91*(3–4), 271–290. https://doi.org/10.1016/j.geomorph.2007.04.023

Crawford, A. M., & Hay, A. E. (2001). Linear transition ripple migration and wave orbital velocity skewness: Observations. *Journal of Geophysical Research*, *106*(C7), 14113–14128. https://doi.org/10.1029/2000JC000612

Dalrymple, R. W., & Rhodes, R. N. (1995). Estuarine dunes and bars. In *Developments in sedimentology* (Vol. 53, pp. 359–422). Elsevier. https://doi.org/10.1016/S0070-4571(05)80033-0

Damgaard, J. S., Whitehouse, R. J., & Soulsby, R. L. (1997). Bed-load sediment transport on steep longitudinal slopes. *Journal of Hydraulic Engineering*, *123*(12), 1130–1138. https://doi.org/10.1061/(ASCE)0733-9429(1997)123:12(1130)

Dean, R. G., & Dalrymple, R. A. (2004). *Coastal processes with engineering applications*. Cambridge University Press. https://doi.org/10.1017/CBO9780511754500

de Schipper, M. A., de Vries, S., Ruessink, G., de Zeeuw, R. C., Rutten, J., van Gelder-Maas, C., & Stive, M. J. F. (2016). Initial spreading of a mega feeder nourishment: Observations of the sand engine pilot project. *Coastal Engineering*, *111*, 23–38. https://doi.org/10.1016/j.coastaleng.2015.10.011

de Schipper, M. A., Hopkins, J., Wengrove, M. E., Saxoni, I., Kleinhans, M., Senechal, N., et al. (2019). Modex: Laboratory experiment exploring sediment spreading of a mound under waves and currents. In *Coastal sediments 2019: Proceedings of the 9th international conference on coastal sediments* (pp. 511–524). https://doi.org/10.1142/9789811204487_0046

de Vriend, H. J. (1987a). 2DH mathematical modelling of morphological evolutions in shallow water. *Coastal Engineering*, *11*(1), 1–27. https://doi.org/10.1016/0378-3839(87)90037-8

de Vriend, H. J. (1987b). Analysis of horizontally two-dimensional morphological evolutions in shallow water. *Journal of Geophysical Research*, *92*(C4), 3877–3893. https://doi.org/10.1029/jc092ic04p03877

Dietrich, W. E., & Smith, J. D. (1984). Bed load transport in a river meander. *Water Resources Research*, *20*(10), 1355–1380. https://doi.org/10.1029/WR020i010p01355

Doucette, J. S., & O'Donoghue, T. (2006). Response of sand ripples to change in oscillatory flow. *Sedimentology*, *53*(3), 581–596. https://doi.org/10.1111/j.1365-3091.2006.00774.x

Engelund, F. (1981). The motion of sediment particles on an inclined bed. *Progress Report*, *53*, 15–20.

Farge, M. (1992). Wavelet transforms and their applications to turbulence. *Annual Review of Fluid Mechanics*, *24*(1), 395–458. https://doi.org/10.1146/annurev.fl.24.010192.002143

Flores, N. Z., & Sleath, J. F. A. (1998). Mobile layer in oscillatory sheet flow. *Journal of Geophysical Research*, *103*(C6), 12783–12793. https://doi.org/10.1029/98JC00691

García-Hermosa, M. I. (2008). *Morphodynamics of sand mounds in shallow flows* (Unpublished doctoral dissertation). Doctoral dissertation, University of Oxford.

Goda, Y. (2010). *Random seas and design of maritime structures* (Vol. 33). World Scientific Publishing Company.

Gutierrez, R. R., Abad, J. D., Parsons, D. R., & Best, J. L. (2013). Discrimination of bed form scales using robust spline filters and wavelet transforms: Methods and application to synthetic signals and bed forms of the Río Paraná, Argentina. *Journal of Geophysical Research: Earth Surface*, *118*(3), 1400–1418. https://doi.org/10.1002/jgrf.20102

Hauguel, A. (1979). Numerical modeling of sediment transport. report no 3. experimental comparison (Tech. Rep.). National Hydraulics and Environment Laboratory (LNHE), EDF.

Hay, A. E., & Mudge, T. (2005). Principal bed states during SandyDuck97: Occurrence, spectral anisotropy, and the bed state storm cycle. *Journal of Geophysical Research*, *110*(C3), C0313. https://doi.org/10.1029/2004jc002451

Hewageegana, V. H., & Canestrelli, A. (2021). On the predictive skill of morphodynamic models for onshore sandbar migration. *Earth Surface Processes and Landforms*, *46*(9), 1692–1712. https://doi.org/10.1002/esp.5079

Jerolmack, D. J., & Mohrig, D. (2005). A unified model for subaqueous bed form dynamics. *Water Resources Research*, *41*(12), W12421. https://doi.org/10.1029/2005WR004329

Jones, K. R., & Traykovski, P. (2019). Interaction of superimposed megaripples and dunes in a tidally energetic environment. *Journal of Coastal Research*, *35*(5), 948–958. https://doi.org/10.2112/JCOASTRES-D-18-00084.1

Kocurek, G., Ewing, R. C., & Mohrig, D. (2010). How do bedform patterns arise? New views on the role of bedform interactions within a set of boundary conditions. *Earth Surface Processes and Landforms*, *35*(1), 51–63. https://doi.org/10.1002/esp.1913

Kranenburg, W. M., Ribberink, J. S., Uittenbogaard, R. E., & Hulscher, S. J. M. H. (2012). Net currents in the wave bottom boundary layer: On wave-shape streaming and progressive wave streaming. *Journal of Geophysical Research*, *117*(F3), F03005. https://doi.org/10.1029/2011JF002070

Lee, S.-B., Wengrove, M., de Schipper, M., Hopkins, J., Kleinhans, M., & Ruessink, G. (2022). "MODEX - processed wave-only series data", in MODEX (MOrphological diffusivity EXperiment) [Dataset]. DesignSafe. https://doi.org/10.17603/ds2-qzkn-7a92

Lee, S.-B., Wengrove, M. E., Hopkins, J., Saxoni, I., & de Schipper, M. A. (2019). Wave driven sand ripple formation and evolution on a mound. In *Coastal sediments 2019: Proceedings of the 9th international conference on coastal sediments* (pp. 615–626). https://doi.org/10.1142/9789811204487_0054

Lefebvre, A., Ernstsen, V. B., & Winter, C. (2013). Estimation of roughness lengths and flow separation over compound bedforms in a natural-tidal inlet. *Continental Shelf Research*, *61*, 98–111. https://doi.org/10.1016/j.csr.2013.04.030

Lesser, G. R., Roelvink, J. A., van Kester, J. A. T. M., & Stelling, G. S. (2004). Development and validation of a three-dimensional morphological model. *Coastal Engineering*, *51*(8–9), 883–915. https://doi.org/10.1016/j.coastaleng.2004.07.014

Longuet-Higgins, M. S. (1983). Wave set-up, percolation and undertow in the surf zone. *Proceedings of the Royal Society of London. A. Mathematical and Physical Sciences*, *390*(1799), 283–291. https://doi.org/10.1098/rspa.1983.0132

Longuet-Higgins, M. S., & Stewart, R. (1964). Radiation stresses in water waves; a physical discussion, with applications. *Deep-Sea Research and Oceanographic Abstracts*, *11*(4), 529–562. https://doi.org/10.1016/0011-7471(64)90001-4

Luque, R. F., & van Beek, R. (1976). Erosion and transport of bed-load sediment. *Journal of Hydraulic Research*, *14*(2), 127–144. https://doi.org/10.1080/00221686709499677

Maier, I., & Hay, A. E. (2009). Occurrence and orientation of anorbital ripples in near-shore sands. *Journal of Geophysical Research*, *114*(F4), F04022. https://doi.org/10.1029/2008JF001126

Masselink, G., Austin, M. J., O'Hare, T. J., & Russell, P. E. (2007). Geometry and dynamics of wave ripples in the nearshore zone of a coarse sandy beach. *Journal of Geophysical Research*, *112*(C10), C10022. https://doi.org/10.1029/2006JC003839

Miles, J., & Thorpe, A. (2015). Bedform contributions to cross-shore sediment transport on a dissipative beach. *Coastal Engineering*, *98*, 65–77. https://doi.org/10.1016/j.coastaleng.2015.01.007

Moulton, M., Elgar, S., & Raubenheimer, B. (2014). A surfzone morphological diffusivity estimated from the evolution of excavated holes. *Geophysical Research Letters*, *41*(13), 4628–4636. https://doi.org/10.1002/2014GL060519

Nielsen, P. (1992). *Coastal bottom boundary layers and sediment transport* (Vol. 4). World scientific.

Nienhuis, J. H., Perron, J. T., Kao, J. C. T., & Myrow, P. M. (2014). Wavelength selection and symmetry breaking in orbital wave ripples. *Journal of Geophysical Research: Earth Surface*, *119*(10), 2239–2257. https://doi.org/10.1002/2014JF003158

O'Donoghue, T., Doucette, J., van der Werf, J. J., & Ribberink, J. S. (2006). The dimensions of sand ripples in full-scale oscillatory flows. *Coastal Engineering*, *53*(12), 997–1012. https://doi.org/10.1016/j.coastaleng.2006.06.008

Passchier, S., & Kleinhans, M. G. (2005). Observations of sand waves, megaripples, and hummocks in the Dutch coastal area and their relation to currents and combined flow conditions. *Journal of Geophysical Research*, *110*(F4), F04S15. https://doi.org/10.1029/2004JF000215

Petrotta, C., Faraci, C., Scandura, P., & Foti, E. (2018). Experimental investigation on sea ripple evolution over sloping beaches. *Ocean Dynamics*, *68*(9), 1221–1237. https://doi.org/10.1007/s10236-018-1197-x

Raja, J., Muralikrishnan, B., & Fu, S. (2002). Recent advances in separation of roughness, waviness and form. *Precision Engineering*, *26*(2), 222–235. https://doi.org/10.1016/S0141-6359(02)00103-4

Ranasinghe, R. (2020). On the need for a new generation of coastal change models for the 21st century. *Scientific Reports*, *10*(1), 1–6. https://doi.org/10.1038/s41598-020-58376-x

Ribas, F., Falques, A., De Swart, H. E., Dodd, N., Garnier, R., & Calvete, D. (2015). Understanding coastal morphodynamic patterns from depth-averaged sediment concentration. *Reviews of Geophysics*, *53*(2), 362–410. https://doi.org/10.1002/2014RG000457

Ruessink, G., Brinkkemper, J. A., & Kleinhans, M. G. (2015). Geometry of wave-formed orbital ripples in coarse sand. *Journal of Marine Science and Engineering*, *3*(4), 1568–1594. https://doi.org/10.3390/jmse3041568

Ruggeri, A., Musumeci, R. E., & Faraci, C. (2020). Wave-current flow and vorticity close to a fixed rippled bed. *Journal of Marine Science and Engineering*, *8*(11), 867. https://doi.org/10.3390/jmse8110867

Ruggiero, P., Kaminsky, G. M., Gelfenbaum, G., & Cohn, N. (2016). Morphodynamics of prograding beaches: A synthesis of seasonal-to century-scale observations of the Columbia River littoral cell. *Marine Geology*, *376*, 51–68. https://doi.org/10.1016/j.margeo.2016.03.012

Saulter, A. N., Russell, P. E., Gallagher, E. L., & Miles, J. R. (2003). Observations of bed level change in a saturated surf zone. *Journal of Geophysical Research*, *108*(C4), 3112. https://doi.org/10.1029/2000JC000684

Sherwood, C. R., Van Dongeren, A., Doyle, J., Hegermiller, C. A., Hsu, T.-J., Kalra, T. S., et al. (2022). Modeling the morphodynamics of coastal responses to extreme events: What shape are we in? *Annual Review of Marine Science*, *14*(1), 457–492. https://doi.org/10.1146/annurev-marine-032221-090215

Simons, D. B., Richardson, E., & Nordin, C. (1965). Sedimentary structures generated by flow in alluvial channels. https://doi.org/10.2110/pec.65.08.0034

Sleath, J. F. A. (1999). Conditions for plug formation in oscillatory flow. *Continental Shelf Researc*h, *19*(13), 1643–1664. https://doi.org/10.1016/S0278-4343(98)00096-X

Sleath, J. F. A., & Rajaona, R. D. (1994). Bedload transport in oscillatory flow. *Sediment transport mechanisms in coastal environments and rivers*, 93–106. https://doi.org/10.1142/9789814533966

Smith, E. R., Mohr, M. C., & Chader, S. A. (2017). Laboratory experiments on beach change due to nearshore mound placement. *Coastal Engineering*, *121*, 119–128. https://doi.org/10.1016/j.coastaleng.2016.12.010

Stansby, P. K., Huang, J., Apsley, D. D., García-Hermosa, M. I., Borthwick, A. G. L., Taylor, P. H., & Soulsby, R. L. (2009). Fundamental study for morphodynamic modelling: Sand mounds in oscillatory flows. *Coastal Engineering*, *56*(4), 408–418. https://doi.org/10.1016/j.coastaleng.2008.09.011

Torrence, C., & Compo, G. P. (1998). A practical guide to wavelet analysis. *Bulletin of the American Meteorological Society*, *79*(1), 61–78. https://doi.org/10.1175/1520-0477(1998)079<0061:APGTWA>2.0.CO;2

Traykovski, P., Hay, A. E., Irish, J. D., & Lynch, J. F. (1999). Geometry, migration, and evolution of wave orbital ripples at LEO-15. *Journal of Geophysical Research*, *104*(C1), 1505–1524. https://doi.org/10.1029/1998jc900026

Van den Berg, N., Falqués, A., & Ribas, F. (2012). Modeling large scale shoreline sand waves under oblique wave incidence. *Journal of Geophysical Research*, *117*(F3), F03019. https://doi.org/10.1029/2011JF002177

van der Werf, J. J., Doucette, J. S., O'Donoghue, T., & Ribberink, J. S. (2007). Detailed measurements of velocities and suspended sand concentrations over full-scale ripples in regular oscillatory flow. *Journal of Geophysical Research*, *112*(F2), F02012. https://doi.org/10.1029/2006JF000614

van Rijn, L. C. (2007). Unified view of sediment transport by currents and waves. i: Initiation of motion, bed roughness, and bed-load transport. *Journal of Hydraulic Engineering*, *133*(6), 649–667. https://doi.org/10.1061/(ASCE)0733-9429(2007)133:6(649)

van Scheltinga, R. C. T., Coco, G., Kleinhans, M. G., & Friedrich, H. (2020). Observations of dune interactions from dems using through-water structure from motion. *Geomorphology*, *359*, 107126. https://doi.org/10.1016/j.geomorph.2020.107126

Wang, D., & Yuan, J. (2018). Bottom-slope-induced net sediment transport rate under oscillatory flows in the rippled-bed regime. *Journal of Geophysical Research: Oceans*, *123*(10), 7308–7331. https://doi.org/10.1029/2018JC013810

Wengrove, M. E. (2018). *Bedform geometry and bedload sediment flux in coastal wave, current, and combined wave-current flows* (Unpublished doctoral dissertation). University of New Hampshire.

Wengrove, M. E., de Schipper, M. A., Lippmann, T. C., & Foster, D. L. (2022). Surfzone bedform migration and sediment flux implications to large scale morphologic evolution. *Geomorphology*, *410*, 108246. https://doi.org/10.1016/j.geomorph.2022.108246

Wengrove, M. E., Foster, D. L., Lippmann, T. C., de Schipper, M. A., & Calantoni, J. (2018). Observations of time-dependent bedform transformation in combined wave-current flows. *Journal of Geophysical Research: Oceans*, *123*(10), 7581–7598. https://doi.org/10.1029/2018jc014357

Wengrove, M. E., Foster, D. L., Lippmann, T. C., de Schipper, M. A., & Calantoni, J. (2019). Observations of bedform migration and bedload sediment transport in combined wave-current flows. *Journal of Geophysical Research: Oceans*, *124*(7), 4572–4590. https://doi.org/10.1029/2018jc014555

Winter, C., Vittori, G., Ernstsen, V. B., & Bartholdy, J. (2008). On the superimposition of bedforms in a tidal channel. *Marine and River Dune Dynamics*, 337–344.

References From the Supporting Information

Higgins, J. P. T., Thomas, J., Chandler, J., Cumpston, M., Li, T., Page, M. J., & Welch, V. A. (2019). *Cochrane handbook for systematic reviews of interventions*. John Wiley and Sons.